Cell Communication and Signaling

RESEARCH Open Access

Induced mitochondrial deficit by NDUFS3 transient silencing reduces RAB7 expression and causes lysosomal dysfunction in pancreatic cancer cells

Giulia Girolimetti[1†], Sinforosa Gagliardi[2†], Paola Cordella[1], Grazia Bramato[2], Riccardo Di Corato[3,4], Roberta Romano[1], Flora Guerra[2†] and Cecilia Bucci[1*†]

Abstract

Background RAB7 is a small GTPase with multiple cellular roles, regulating late endocytic trafficking and lysosomal biogenesis, influencing mitochondria-lysosome crosstalk, and contributing to many mitochondrial processes. Mitochondrial dysfunctions are widely reported in cancer and the development of cancer therapeutic strategies targeting mitochondria gained momentum in recent years. Mitochondrial impairment can cause alterations of mitochondria-lysosome crosstalk and can influence lysosomal function. Here, we used cell models of pancreatic cancer, one of the deadliest cancers worldwide, to cause a transient mild mitochondrial deficit lowering NDUFS3 protein levels in order to investigate the consequences on RAB7 and on the late endocytic pathway and, thus, the contribution of the mitochondria-lysosomes communication alterations to cancer progression.

Methods NDUFS3 and RAB7 downregulation was obtained by RNA interference (RNAi). Seahorse assays, Western blot analysis, mitochondrial staining, and Transmission Electron Microscopy (TEM) were used to assess silencing effects on mitochondrial structure and functioning. Western blotting was used to investigate expression of late endocytic pathway proteins and of the invasion marker vimentin. Confocal microscopy was used to analyze the mitochondrial network and lysosomal assessment. Zymography was performed to evaluate the ability to digest the extracellular matrix linked to cancer migration. SRB and colony assays were performed to assess cancer viability and proliferation. Wound healing assay and FluoroBlok membranes were used to determine migration and invasiveness.

Results In pancreatic cancer cells, transient silencing of the NDUFS3 protein caused mitochondrial deficit, slower oxidative metabolism, and mitochondrial morphology alterations. In this context, we observed RAB7 downregulation and impairment of the late endocytic pathway. In addition, *NDUFS3*-silenced RAB7-downregulated cells showed less

†Giulia Girolimetti and Sinforosa Gagliardi contributed equally to this work as co-first authors.

†Flora Guerra and Cecilia Bucci contributed equally to this work as co-last authors.

*Correspondence:
Cecilia Bucci
cecilia.bucci@unisalento.it

Full list of author information is available at the end of the article

invasive tumorigenic potential revealed by reduced levels of vimentin and other Epithelial-to-Mesenchymal Transition proteins, decreased viability, migration and invasiveness. Moreover, we found that modulation of RAB7 expression may regulate vimentin levels and influence mitochondrial morphology and levels of mitochondrial proteins.

Conclusions Overall, our data show that mitochondrial deficit determines alterations of the crosstalk with lysosomes, leading to dysfunctions, and that this process is regulated by RAB7 acting as an oncogene. This highlights the synergic role of RAB7 and mitochondrial dysfunction, focusing on a cellular mechanism that may boost the effect of mitochondrial dysfunction in the cells, leading to the reduction of the tumorigenic potential.

Keywords RAB7, Mitochondria, Lysosomes, Endocytosis, Pancreatic cancer

Introduction

RAB7A (hereafter referred to as RAB7) is a small GTPase with multiple cellular roles as it regulates trafficking from early endosomes (EE) to lysosomes, EE maturation, lysosomal biogenesis, and clustering and fusion of late endosomes (LE) and lysosomes in the perinuclear region [1, 2]. RAB7 also plays a role in many mitochondrial processes, such as mitophagy [3], mitochondrial fusion and fission [4–6], mitochondrial protein translation [7], and mitochondria-derived vesicle (MDV) biogenesis [8] and secretion [9]. Guanosine triphosphate (GTP) hydrolysis by RAB7 promotes the untethering of mitochondria-lysosome contact sites, influencing their duration, number, and frequency [5], thus making RAB7 fundamental for these interactions. The alterations of the crosstalk between mitochondria and lysosomes have been reported in cancer and neurodegenerative diseases [10–13]. Importantly, mitochondrial impairment can influence lysosomal function and *viceversa* [10]. Targeting mitochondria is a promising strategy for cancer therapy. Indeed, due to the mitochondrial bioenergetic and biosynthetic function, in the context of cancer, mitochondria are considered the metabolic hub of cell proliferation, survival, and metastasis [14].

Despite the "Warburg effect," in which cancer cells rely primarily on glycolysis rather than mitochondrial oxidative phosphorylation (OXPHOS) even in aerobic conditions, how mitochondrial dysfunction contributes to cancer progression is still debated [15]. Recent findings in cancer metabolism have highlighted promising metabolic targets that could affect cancer progression, invasiveness, metastasis formation, and response to therapies [16, 17]. In this context, mitochondrial complex I (CI), the first and rate-limiting enzyme of the OXPHOS system, appears to be a particularly promising candidate for developing anticancer strategies [18–20]. CI function was explored using potent inhibitors that severely impact respiratory chain function and cell metabolism resulting in the suppression of tumor growth and progression [21–23]. NDUFS3 is a subunit of CI already characterized in cancer, highly conserved across evolution, and believed to be essential for CI assembly. Indeed, NDUFS3 ablation causes CI-deficient tumors as the knock-out of *NDUFS3* in *vitro* models of two different cancer types induces a severe decrease of CI activity and blocks mitochondrial respiration, resulting in a major OXPHOS defect and cancer indolence [18].

Thus, given the role of RAB7 in mitochondria-lysosomes communication, we used pancreatic cancer cell lines to assess the effect of the mitochondrial deficit caused by reduced levels of NDUFS3 transiently silenced on RAB7 and, consequently, on the late endocytic pathway and lysosomes. RAB7 has been described as a tumor suppressor or as an oncogene [24] in the context of cancer progression, depending on cellular and environmental context. Still, its role in the context of dysfunctional mitochondria in cancer has not yet been clarified. Here, we provide evidence that in *NDUFS3*-silenced cells, RAB7 is downregulated and, consequently, the late endocytic pathway and lysosomes are impaired. Furthermore, although we silenced NDUFS3 transiently, we observed a reduction in cellular viability, colony formation capacity, and vimentin levels compared to controls, indicating that the decrease in CI and the mitochondrial deficit is sufficient to attenuate aggressiveness and epithelial-mesenchymal transition in these cells by a RAB7-dependent process, thus inducing a less aggressive phenotype.

Materials and methods

Cell lines and treatments

Two different pancreatic cancer cell lines, MIA PaCa-2 (Cellosaurus Research Resource Identifiers RRID: CVCL_0428) [25] and YAPC (RRID: CVCL_1794) [25] cells were grown in DMEM (Euroclone, Milano, Italy). Media were supplemented with 10% FBS, 2 mM glutamine, 100 U/mL penicillin, and 10 mg/mL streptomycin (Euroclone, Milano, Italy). Cell lines were grown in a 5% CO_2 incubator at 37 °C. MIA PaCa-2 cells were kindly provided by Prof. Miriam Martini (University of Turin, Turin, Italy) [26], while YAPC cells were a gift from Dr. Loredana Moro (Memorial Sloan Kettering Cancer Center, NY, USA) [27]. Where indicated, cells were treated with MG132 (20 μM, Sigma-Aldrich, MO, USA), cycloheximide (CHX) (50 μM, Sigma-Aldrich) for 2 h and 4 h, with Rotenone (1 μM, Santa Cruz, CA, USA) for 48 h (YAPC) and 72 h (MIA PaCa-2), and with carbonyl

cyanide m-chlorophenyl hydrazone (CCCP) (10 μM, Enzo Life Science, NY, USA) for 18 h.

RNA interference and transfection

NDUFS3 silencing was performed using Metafectene SI$^+$ from Biontex (Martinsried, Germany) as indicated by the manufacturer. Control RNA (Scrambled, Scr), NDUFS3, and RAB7 small interfering RNAs (siRNAs) were purchased from Eurofins Genomics (Ebersberg, Germany). Control RNA and RAB7A siRNA efficiency were previously reported [28]. For NDUFS3 silencing, two different siRNAs (siRNA #1 and siRNA #2) were used. The sequences of all siRNAs used are indicated in supplementary Table S2. For all subsequent experiments, after 48 h from silencing medium was replaced and cells were seeded for further analyses or processed. siRNAs efficiency in NDUFS3 silencing and RAB7 protein levels were tested by Western blotting at different times (for YAPC cells 3, 5, 7 and 9 days; for MIA PaCa-2 cells 3,5, 7, 9 and 11 days).

Cells were transiently transfected with K4 Transfection System from Biontex (Martinsried, Germany) according to the manufacturer's protocol. Plasmids pcDNA3.1 vector (Invitrogen, V79020) encoding 2xHA and 2xHA-RAB7A wild type were previously described [29]. Briefly, after 48 h of NDUFS3 silencing, YAPC and MIA PaCa-2 cells were seeded and then transfected at day 3 for 18 h. Then, the medium was replaced, and cells were collected and used for Western blot analysis after 7 and 9 days from silencing for YAPC and MIA PaCa-2 cells, respectively.

DQ-BSA (Self-Quenched BODIPY dye conjugates of bovine serum Albumin) assay

Cells were seeded on coverslips in a 24-well plate to achieve 70–80% confluency and treated with 50 μg/ml Green DQ-BSA (# D12050, ThermoFisher Scientific, Carlsbad, CA, USA) for 24 h. Glass coverslips were fixed with 3% paraformaldehyde for 20 min, washed with PBS (Phosphate Buffered Saline), and stained with 4′,6-diamidino-2-phenylindole (DAPI). Cells were imaged using Zeiss LSM 900 confocal laser scanning microscope (CLSM) (Germany) and quantitative analysis was performed on at least 50 cells per sample using NIH ImageJ (Bethesda, MD, USA).

Live imaging confocal microscopy

For live imaging assay, cells were seeded in 8 well μ-slide microscopy chambers (Ibidi GmBh, Martinsried, Germany). After 24 h cells were treated with 20 nM of PureBluTM Hoechst 33,342 Nuclear Staining Dye (BioRad) and 100 nM LysoTracker Red DND-99 (Thermofisher) as previously described [9, 30]. Similarly, we stained mitochondria with 50 nM MitoTracker Green FM (Thermofisher), as previously described [30, 31].

After 3 washes in PBS, L-15 medium (Leibowitz medium without phenol red, Gibco, TermoFisher) was added and cells were imaged by confocal microscopy. Images were captured using CLSM (Zeiss, LSM 900, Germany) equipped with a laser diode emitting at 405 nm, an argon-ion laser for excitation at 488 nm, and a helium-neon laser for excitation at 555 nm. Images were taken with a Plan-Apochromat 63.0 × 1.40 oil-immersion objective DIC M27. Live imaging assay results were analyzed by ImageJ (Bethesda, MD, USA).

Western blotting

Cells were lysed with Laemmli buffer (100 mM Tris–HCl pH 6.8, 4% SDS, 20% glycerol, and 0.2% blue bromophenol) and then quantified using the BCA assay (Thermofisher Scientific). All antibodies used are listed in Supplementary Table S1. Secondary antibodies conjugated with horseradish peroxidase (HRP) are used at 1:5000 dilution for immunoblot.

Images were acquired by the ChemiDoc MP Imaging System and analyzed by Image Lab TM software version 6.0.1 (Bio-Rad Laboratories). Protein expression levels were quantified by densitometry normalizing against Heat shock protein HSP 90-alpha (HSP90) housekeeping protein.

Gelatin zymography

The gelatin zymography assay was performed using 30 μg of each sample as previously described [32]. Briefly, the serum-free medium of the cultured cells was collected and concentrated after 24 h. The secreted proteins were separated under non-reducing conditions in a polyacrylamide gelatin gel. The gelatin-digested zone, shown as a clear area on a blue background, is observed after Coomassie Blue staining.

Maturation of cathepsin D

Maturation of Cathepsin D was evaluated through Western blot analysis using an anti-Cathepsin-D antibody (Santa Cruz Biotechnology) that recognizes, not only the 32 kDa mature form but also the 52 kDa and 44-kDa immature forms. Protein levels were quantified by densitometry with Image Lab TM software version 6.0.1 (Bio-Rad) and the amount of maturation was expressed as the ratio between immature forms (52/44 kDa) and mature form (32 kDa) [30].

Measurement of mitochondrial morphology and network complexity

Cells were seeded on 11 mm round glass coverslips in 24 well plates to achieve 70–80% confluency. After 24 h, cells were incubated with 75 nM MitoTracker Red CMXRos (ThermoFisher Scientific) for 45 min at 37 °C. After 3 washes in PBS, cells were fixed with 3% paraformaldehyde

for 15 min at 37 °C, incubated with NH_4Cl 50mM for 10 min, washed 3 times with PBS 1X and then incubated with DAPI for 5 min. Finally, coverslips were mounted on a drop of Mowiol (Calbiochem-Nova biochem Corporation, La Jolla, CA, USA). Fluorescence images were captured using CLSM (Zeiss, LSM 900, Germany) described above.

The width and height of individual mitochondria were measured, and the aspect ratio was a measurement for mitochondrial size. Established methods for multidimensional measurements of mitochondrial morphology were used to quantify the mitochondrial size and network complexity [33, 34]. The Mitochondria Analyzer plugin can be downloaded from http://sites.imagej.net/ACMito/ and installed in Fiji of NIH ImageJ. Briefly, healthy mitochondria are generally mobile and tubular in shape and exist in complex networks, whereas cells undergoing profound stress or entering apoptosis often display swollen and fragmented mitochondria. Thus, the mitochondria analyzer is designed to measure both the size, the shape of the individual mitochondrion, and network complexity. The mitochondrial size can be measured in area and perimeter. The shape is reflected by the aspect ratio (maximal: minimal diameter) and by the form factor. The complexity of the mitochondrial network is revealed by the number of branch joints, branches and branch length.

Following the instructions in Chaudhry et al., [34], we defined the mitochondrial morphology to three different levels of complexity: Level 1 (L1) was for the highly complex mitochondrial network with little or no fragmented mitochondria; Level 2 (L2) represented less complex mitochondrial network with fragmented mitochondria; Level 3 (L3) was for highly fragmented mitochondria with little or no network. For 2D analysis, the image was first processed and thresholded. The blocking size of 1.05/1.25/1.45 µm and C-value of 5/9/13 were applied for L1, L2, and L3, respectively). The resulting binary image was used as the input for the "analyze particles" command (size = 100/70/40 pixels -infinity, circularity = 0.00–1.00, for level 1/2/3). Note that only mitochondria larger than 100/70/40-pixel units were taken into consideration in those 3 conditions, respectively. The output measurements generated for "area" and "perimeter" represented the average size of mitochondria. The shape of mitochondria was revealed by the values for both the aspect ratio (AR) and the Form Factor (FF). FF was derived as the inverse of the "circularity" output value to take into consideration of curvatures.

Quantitative Real-Time PCR

Standard RNA procedures and quantitative Real-Time PCR (qRT-PCR) were performed as previously described [35]. Total RNA was extracted from MIA PaCa-2 and YAPC cell lines after 3, 5, 7, 9, and 11 days from *NDUFS3* silencing and their controls using TRIzol Reagent (Thermo Fisher Scientific, Waltham, MA, USA) according to the manufacturer's instructions. Quality control and quantification of the extracted RNA were performed using a NanoDrop ND-1000 spectrophotometer (Thermo Scientific, Waltham, MA, USA). Reverse transcription of 500 ng of RNA was performed using an iScript cDNA Synthesis kit (Bio-Rad). Quantitative Real-Time PCR for RAB7 was performed with SsoAdvanced Universal SYBR Green Supermix (Bio-Rad) on a CFX96 TouchTM Real-Time PCR Detection System (Bio-Rad). RAB7 levels were normalized to RPLP0 levels, used as a housekeeping gene, and relative mRNA expression was calculated using the ΔΔCt method and expressed as "fold change". The specificity of PCR products was confirmed by melting curve analysis. Primer sequences are reported in Table S2.

Transmission Electron microscopy (TEM)

Cells monolayers were rinsed with PBS, fixed using 2.5% glutaraldehyde at 4 °C and then post-fixed with 1% osmium tetroxide containing 1.5% potassium cyanoferrate. Afterward, the cellular monolayers were gradually dehydrated in ascending concentrations of ethanol and embedded in Epon resin. Thin sections of 80 nm were obtained using an ultramicrotome and collected onto copper TEM grids. The grids were finally stained by UranyLess EM Stain (Electron Microscopy Sciences), by following the standard protocol provided by the manufacturer. TEM analysis was performed with a JEOL JEM-1011 transmission electron microscope at 100 kV operating voltage, equipped with a 7 megapixel CCD camera (Orius SC600A, Gatan, Pleasanton, CA). TEM image analysis was achieved with Gatan Digital Micrograph™ (DM) software. Statistical analysis of the mitochondria size was performed analyzing at least 120 individual mitochondria.

Cell viability measurements

Cell viability of YAPC and MIA PaCa-2 *NDUFS3* silenced and Scr control cells were assessed using the Sulforhodamine B (SRB) assay (Sigma-Aldrich) based on the measurement of cellular protein content. After 48 h from silencing, cells were seeded in 96-well plates (1500 cells/well) in a complete medium. Plate reading was performed on a Multilabel Plate Reader (Victor X5, PerkinElmer, Waltham, MA, USA) at 570 nm. The viability of YAPC and MIA PaCa-2 cells was calculated respectively after 7 and 9 days from *NDUFS3* silencing, comparing silenced cells with Scr cells.

Clonogenic assay

Anchorage-dependent cell growth capacity was determined for YAPC and MIA PaCa-2 *NDUFS3* silenced and

Scr control cells. After 48 h from silencing, suspensions of cells (400 cells) were placed in duplicate in a 32-mm dish and incubated at 37 °C in a humidified 5% CO_2 atmosphere. Colonies formed by YAPC and MIA PaCa-2 cells, respectively, after 7 and 9 days from *NDUFS3* silencing, were fixed, stained, and analyzed. Images of the 32-mm dish were acquired using EVOS™ FL Auto 2 Imaging System (Thermo Fisher Scientific), scanning the entire area of each well, and acquiring multiple images to build a single stitched image for each well. Colonies were counted using ImageJ (Bethesda, MD, USA).

Migration assay using FluoroBlok insert

Migration of *NDUFS3*-silenced YAPC and MIA PaCa-2 was assessed using Corning FluoroBlok 24-multiwell insert plates (6.5 mm diameter) with 8.0 µm pores (Corning, MA, USA). Before seeding, nuclei of cells were stained with 20 nM of PureBluTM Hoechst 33,342 Nuclear Staining Dye (Bio-Rad). DMEM containing 10% FBS was added to the lower chamber of FluoroBlok culture plates. 10^5*NDUFS3*-silenced YAPC and MIA PaCa-2 cells and their respective scrambled controls were seeded into the upper chamber of Corning FluoroBlok insert in serum-free DMEM. Following incubation for 24 h in a 5% CO2 incubator at 37 °C, migration was assayed by fluorescence of cells passing through the microporous membrane. EVOS™ FL Auto 2 Imaging System (Thermo Fisher Scientific) was used to acquire images of fluorescent cells that had traversed the membrane. Using ImageJ (Bethesda, MD, USA), the mean number of cells was calculated in 10 random fields (magnification 10X).

Wound healing assay

Wound healing assay was performed on *NDUFS3*-silenced YAPC cells compared to the Scr control. Cells were seeded in a two-well culture silicone insert (75 × 104 cells/well) with a defined cell-free gap of 500 µm (Ibidi, Germany). Once the cells reached 100% confluence, the silicone insert was removed and the cells were cultured for 24 h. Images of the wound area, clear of cells in the well, were taken with EVOS™ Imaging System (Thermo Fisher Scientific) at 0 (T0) and 24 h after wounding. The wound areas were measured with ImageJ (Bethesda, MD, USA). The migration rate was calculated as the change in the wound area over time and expressed as the percentage of wound closure between 0 and 24 h for the two different conditions. A high wound closure percentage represents the cell line with more migration capacity over time [36].

Seahorse XF oxygen consumption rate (OCR) assay

To evaluate mitochondrial respiration in YAPC and MIA PaCa-2 *NDUFS3* silenced and Scr control cells, the Mito Stress Test Kit (Agilent Technology, CA, USA) was used following the manufacturer's instructions and the oxygen consumption rate (OCR) was measured using the Seahorse XFp Extracellular Flux Analyzers (Agilent Technology) as previously reported [9]. Cells were seeded into an 8-well Seahorse XFp Cell Culture Miniplate (Agilent Technology) at the density of 3×10^4 cells/well in DMEM complete medium and allowed to attach at 37 °C in a humidified incubator with 5% CO_2. The Mito stress test foresees the sequential injection of the following drugs: Oligomycin (1 µM), Carbonyl cyanide-p-trifluoromethoxyphenylhydrazone (FCCP) (1 µM) and Rotenone/Antimycin A (0.5 µM). Three measurements of OCR were obtained for each drug injection. At the end of each experiment, the amount of total cell proteins/well was determined using the BCA assay quantification method (Thermofisher Scientific) described above. The OCR data were analyzed by Seahorse Analytics software, expressed as pmoles of O2 per minute (OCR), and normalized to total protein levels in each well.

Statistical analysis

All experiments were conducted at least 3 times and results are expressed as mean value ± standard error (SEM) (error bars). GraphPad Prism software (Version 10.0) was used to generate the graphs. The statistical significance was determined for all experiments through Student's t-test for unpaired data (*$p \leq 0.05$, **$p \leq 0.01$, and ***$p \leq 0.001$). Fluorescence intensity was evaluated by quantifying Correct Total Cell Fluorescence (CTCF); the number and size of acid compartments and DQ-BSA puncta in cells were determined through the "Analyze Particles" tool of ImageJ. For all measures, at least 50 cells/samples were analyzed for at least three independent experiments. Results are represented as mean ± standard error (SEM).

Results

Transient silencing of *NDUFS3* causes a decrease in mitochondrial subunit expression and bioenergetic deficit

It was already demonstrated that CI ablation caused by genetic *NDUFS3* knock-out in mesenchymal and epithelial cancer cells induces a low-proliferative cancer phenotype and converts malignant cancers in oncocytomas [18]. CI function was also reduced using inhibitor drugs that impact respiratory chain function and cell metabolism [21–23]. To understand the effects of mitochondrial deficit on mitochondria-lysosome communication and on lysosomal function, transient siRNA-mediated silencing of the nuclear-encoded mitochondrial *NDUFS3* gene was carried out. We used two different siRNAs, named siRNA#1 and siRNA#2, in two different pancreatic cancer cell lines, YAPC and MIA PaCa-2 (Fig. 1A and C). Both siRNAs exhibit a high efficiency in reducing NDUFS3 protein levels, lasting up to 9 and 11 days

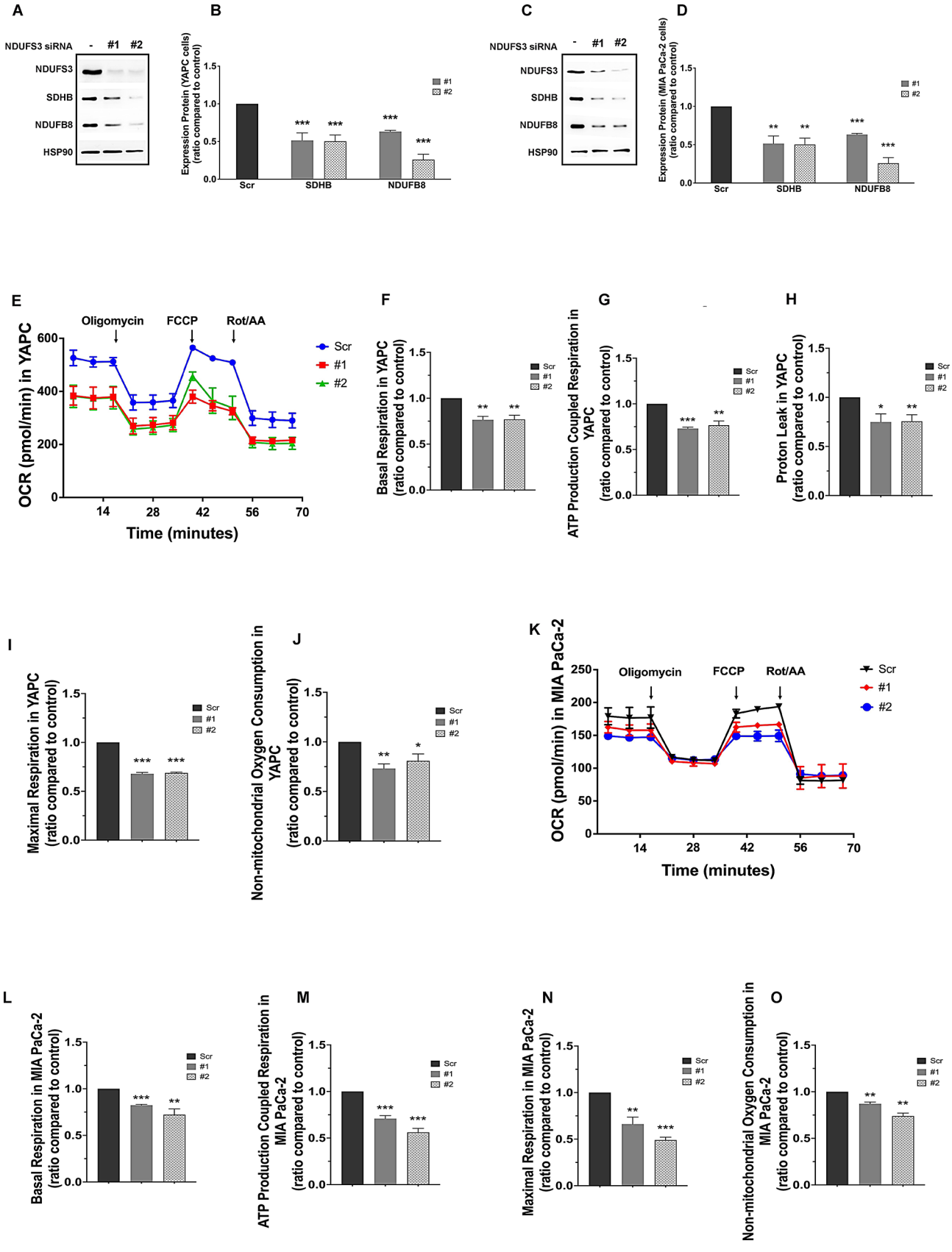

Fig. 1 (See legend on next page.)

(See figure on previous page.)

Fig. 1 Alteration of mitochondrial proteins and function in *NDUFS3*-silenced YAPC and MIA PaCa-2 cells. (**A**-**B**) YAPC and (**C**-**D**) MIA PaCa-2 cells were treated with control RNA (Scrambled, Scr) or with two different *NDUFS3* siRNAs (indicated as #1 and #2) and the expression of mitochondrial proteins was evaluated by Western blotting. The efficiency of RNA interference (RNAi) was verified using an antibody against NDUFS3 and HSP90, as loading control. The relative abundance of SDHB and NDUFB8 protein levels was determined through densitometric analysis using Image Lab Software version 6.0.1 normalizing against HSP90 and was reported as the ratio of *NDUFS3*-silenced cells (#1 and #2) compared to their control (Scr). (**E**) Mitochondrial function was analyzed in *NDUFS3*-silenced (#1 and #2) and control (Scr) YAPC cells with the Seahorse Mito stress kit assay. Oxygen consumption rate (OCR) was measured by Agilent Seahorse XF HS Mini analyzer. Basal respiration (**F**), ATP-production coupled respiration (**G**), proton leak (**H**), maximal respiration (**I**) and non-mitochondrial oxygen consumption (**J**) were determined by data elaboration with Agilent Seahorse Analytics software. (**K**) Mitochondrial function was analyzed in *NDUFS3*-silenced (#1 and #2) and control (Scr) MIA PaCa-2 cells with the Seahorse Mito stress kit assay. Oxygen consumption rate (OCR) was measured by Agilent Seahorse XF HS Mini analyzer. Basal respiration (**L**), ATP-production coupled respiration (**M**), maximal respiration (**N**) and non-mitochondrial oxygen consumption (**O**) were determined by data elaboration with Agilent Seahorse Analytics software. Values are the mean ± SEM of at least three independent experiments. *$p \leq 0.05$, ** $p \leq 0.01$ and *** $p \leq 0.001$

for YAPC and MIA PaCa-2 cells, respectively (Figure S1). In YAPC and MIA PaCa-2 *NDUFS3*-silenced cells we also found that the mitochondrial NADH: Ubiquinone Oxidoreductase Subunit B8 (NDUFB8), a protein of CI, and SDHB, a protein of Complex II (CII), were decreased compared to their respective scrambled (Scr) controls (Fig. 1A-D). To ensure that the *NDUFS3* siRNA-mediated silencing results in an actual functional deficit, the bioenergetic competence of YAPC and MIA PaCa-2 *NDUFS3*-silenced cells and Scr controls was determined using Seahorse Mitostress kit assay (Fig. 1E-O). We found that Oxygen Consumption Rate (OCR) was decreased in both *NDUFS3*-silenced cell lines compared to their controls (Fig. 1E and K). In particular, we observed that Basal respiration, ATP production, Proton Leak, Maximal Respiration, and Non-mitochondrial OCR were significantly reduced in YAPC cells silenced with both NDUFS3 siRNAs (Fig. 1F-J). In MIA PaCa-2 *NDUFS3*-silenced cells we found a significant reduction in Basal respiration, ATP production, Maximal Respiration, and Non-mitochondrial OCR (Fig. 1L-O). These results highlight that transient *NDUFS3*-silencing is sufficient to induce a bioenergetic deficit and a slower oxidative metabolism.

NDUFS3-silenced cell lines show alterations in mitochondrial morphology

With the aim of investigating the effect of the transient *NDUFS3*-silencing on mitochondrial morphology, we performed mitochondrial staining using MitoTracker Red CMXROS dye (Fig. 2A and J). Raw images were processed with the Mitochondria Analyzer in Fiji/ImageJ, as described in the Materials and Methods, to quantify the changes in *NDUFS3*-silenced cells compared to their controls. Notably, network connectivity is critical for remodeling mitochondrial morphology and activity [37], and the numbers of branch junctions per mitochondrion, which is a measurement of network connectivity, were also evaluated as previously described [33, 34]. As shown in Fig. 2, in *NDUFS3*-silenced cells we observed a decrease in the mitochondrial network complexity. Our analyses have revealed that mitochondria in *NDUFS3*-silenced YAPC cells exhibited a significant reduction in the mean area (Fig. 2B) and perimeter (Fig. 2C). In addition, the form factor (Fig. 2E), the branch junctions for mitochondrion (Fig. 2F), the branches for mitochondrion (Fig. 2G), the total length of branches (Fig. 2H) as well as the average branch length (Fig. 2I) were also reduced compared to the scrambled counterpart. In parallel, we found that in MIA PaCa-2 cells the mean area (Fig. 2K), the mean perimeter (Fig. 2L), and the form factor (Fig. 2N) of the mitochondria were reduced after silencing of *NDUFS3* compared to controls. Furthermore, mitochondria, on average, showed a significant reduction in the branch junction and the branches for mitochondrion (Fig. 2O-P), in the total length of branches (Fig. 2Q) as well as in the average branch length (Fig. 2R). Hence, both cell lines showed alterations of mitochondrial morphology in the presence of *NDUFS3* silencing.

Moreover, we evaluated mitochondrial morphology also by electron microscopy (Fig. 3A) measuring the mitochondrial short axis and counting cristae, revealing that *NDUFS3*-silenced YAPC cells were characterized by a significant decrease in the number of cristae and an increase in short mitochondrial axis width while in MIA PaCa-2 cells the same trend was observed although not reaching statistical significance (Fig. 3B-E). Finally, confocal microscopy live imaging assay using MitoTracker Green FM showed that in both *NDUFS3* silenced cell lines, mitochondrial mass was significantly reduced (Fig. 3F-H).

Taken together, these results provided strong evidence that mitochondrial deficit can induce significant mitochondrial fragmentation, leading to a reduction in both the mitochondrial network complexity and the mitochondrial size.

Silencing of *NDUFS3* gene causes downregulation of RAB7 and other proteins of the late endocytic pathway

Emerging evidence suggests that RAB7 is the main regulator of mitochondria-lysosome interorganellar communication [4, 5]. In particular, mitochondrial-lysosomal crosstalk has been widely studied in neurodegeneration [10], while its implication in cancer is still unclear. To understand whether a mitochondrial deficit may cause

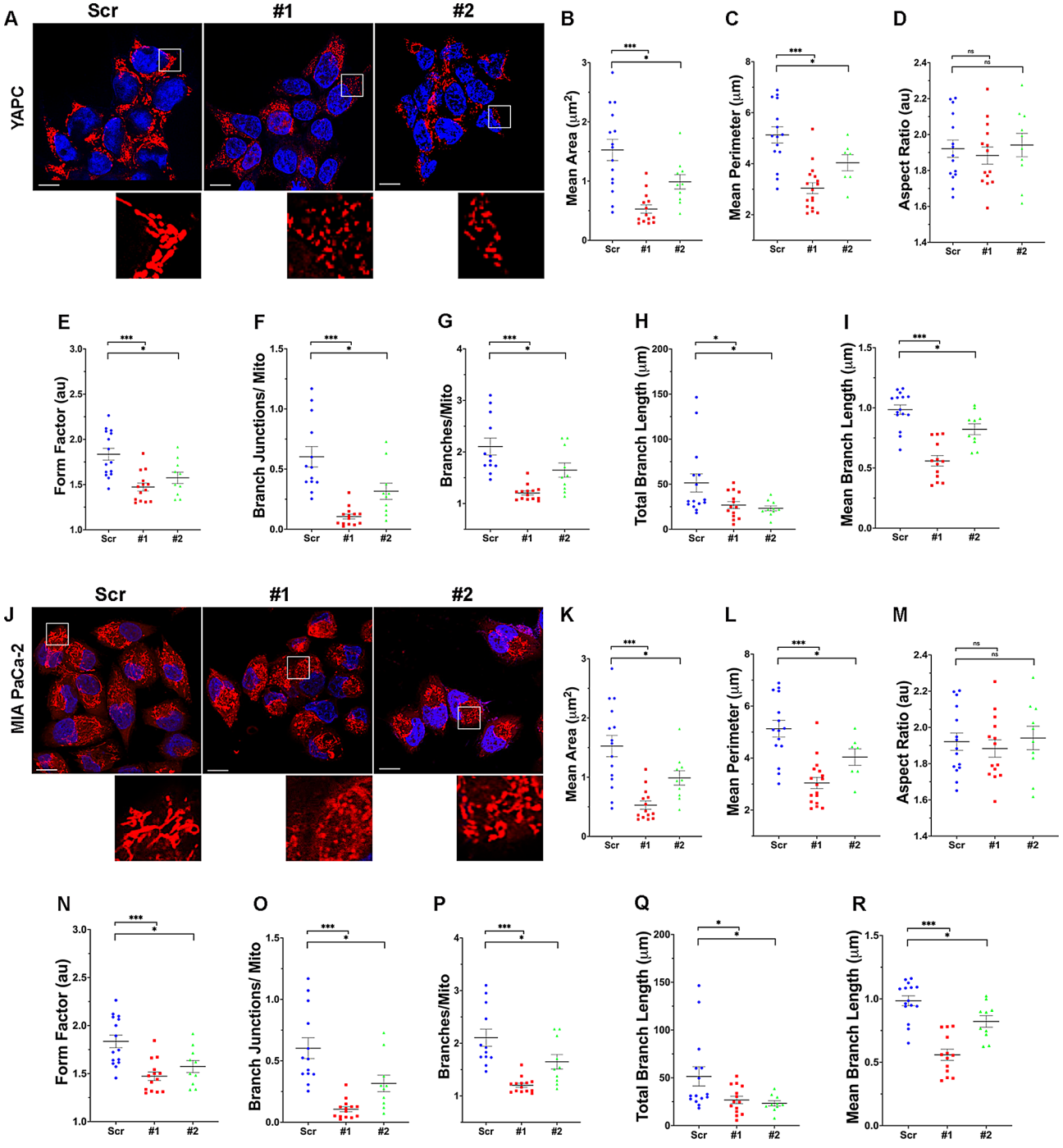

Fig. 2 Alteration of mitochondrial network and morphology in *NDUFS3*-silenced YAPC and MIA PaCa-2 cells. **(A)** Representative images of mitochondria stained with MitoTracker Red CMXROS dye from YAPC cells transfected with control RNA (Scr) or with two different *NDUFS3* siRNAs (#1 and #2). Nuclei were labeled with DAPI (blue). White boxes indicate zoomed areas below. Scale bar: 10 μm. The images were analyzed and quantified using the Mitochondria Analyzer in Fiji/ImageJ software (ImageJ). The measurements for **(B)** Mean Area (μm^2), **(C)** Mean Perimeter (μm), **(D)** Aspect Ratio (au), (**E**) Form Factor (au), **(F)** Branch Junctions/Mito, **(G)** Branches/Mito, **(H)** Total Branch Length (μm) and **(I)** Mean Branch Length (μm) are presented. The numbers of mitochondria analyzed are $n = 3954$ from 15 images for the Scr control group, $n = 5683$ from 19 images for siRNA#1, and $n = 2771$ from 10 images for siRNA#2 transfected cells. **(J)** Representative images of mitochondria stained with MitoTracker Red CMXROS dye from MIA PaCa-2 cells transfected with control RNA (Scr) and with two different *NDUFS3* siRNAs (#1 and #2). Nuclei were labeled with DAPI (blue). White boxes indicate zoomed areas below. Scale bar: 10 μm. The images were analyzed and quantified using the Mitochondria Analyzer in Fiji/ImageJ software (ImageJ). The measurements for **(K)** Mean Area (μm^2), **(L)** Mean Perimeter (μm), **(M)** Aspect Ratio (au), **(N)** Form Factor (au), **(O)** Branch Junctions/Mito, **(P)** Branches/Mito, **(Q)** Total Branch Length (μm) and **(R)** Mean Branch Length (μm) are presented. The numbers of mitochondria analyzed are $n = 3699$ from 16 images for Scr control group, $n = 3361$ from 10 images for siRNA#1, and $n = 4517$ from 20 images for siRNA#2 transfected cells. Values are the mean ± SEM of at least three independent experiments. Abbreviation: ns: not significant. *$p \leq 0.05$, ** $p \leq 0.01$ and *** $p \leq 0.001$

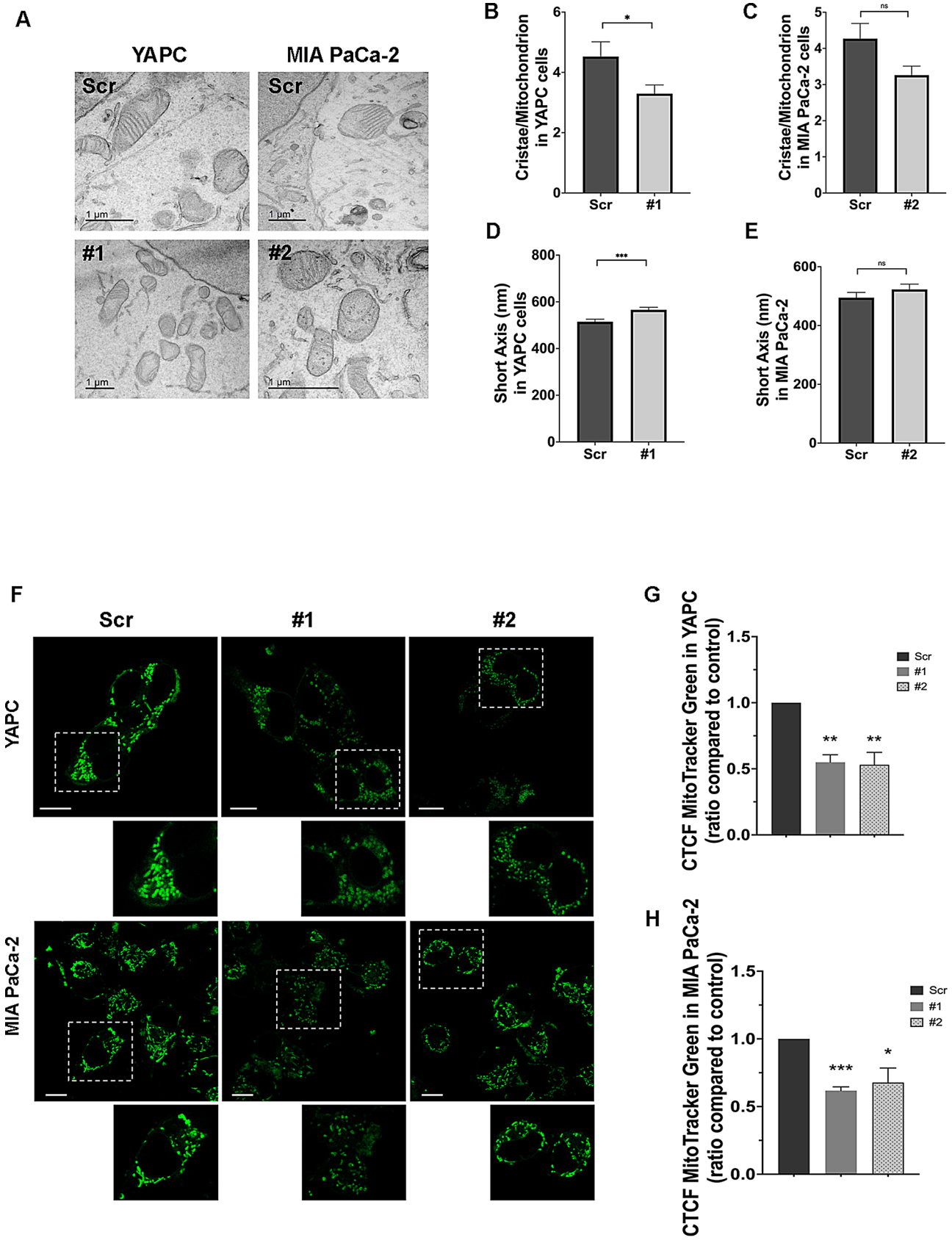

Fig. 3 (See legend on next page.)

(See figure on previous page.)

Fig. 3 Differences in mitochondrial morphology in *NDUFS3*-silenced YAPC and MIA PaCa-2 cells compared to controls. **(A)** Representative electron micrographs of YAPC and MIA PaCa-2 cells transfected with siRNA#1 and siRNA#2, respectively, or with control RNA (Scr). Scale bars: 1 µm. **(B-C)** Evaluation of the *cristae* number and **(D-E)** of the short mitochondrial axis width in *NDUFS3*-silenced YAPC and MIA PaCa-2 cells (indicated as #1 and #2, respectively) compared to their Scr control. (**F**) Mitochondria were live stained in *NDUFS3*-silenced YAPC and MIA PaCa-2 cells (indicated as #1 and #2) and relative Scr controls using MitoTracker Green FM dye. White boxes indicate zoomed areas below. Scale bar: 10 µm. **(G-H)** Corrected total cell fluorescence (CTCF) of mitochondria was determined by ImageJ software in *NDUFS3*-silenced YAPC and MIA PaCa-2 cells and reported as the ratio compared to their Scr control. Each measure was obtained by analyzing at least 50 cells/samples from three or more independent experiments. Values are the mean ± SEM of at least three independent experiments. *$p \le 0.05$, ** $p \le 0.01$ and *** $p \le 0.001$

alterations in lysosomal functions, siRNA-mediated silencing of the nuclear-encoded mitochondrial gene *NDUFS3* was carried out, and first of all, expression levels of endocytic pathway proteins, including RAB7, were analyzed. The results revealed that both *NDUFS3*-silenced cell lines were characterized by a significant downregulation of RAB7 of about 50% (Fig. 4A-D). In previous work, it was demonstrated that the progressive decrease of NDUFS3 affected complex I stability at different times based on the type of cells [38]. Accordingly, we observed that RAB7 underwent the most relevant significant downregulation after 7 days in YAPC, and after 9 days in MIA PaCa-2 cells upon *NDUFS3* silencing (Figure S1).

Then, we investigated if RAB7 downregulation in *NDUFS3*-silenced cells was due to an increase in proteasomal degradation or alteration of protein stability by inhibiting the proteasome with MG132 or protein translation with cycloheximide, respectively (Figure S2). We found no change in the amount of RAB7 protein after proteasome or protein translation inhibitions in YAPC (Figure S2 A-D) and MIA PaCa-2 (Figure S2 E-H) silenced cell lines. Furthermore, we analyzed RAB7 mRNA levels by qRT-PCR, and even in this case, we found no changes after *NDUFS3* silencing in both pancreatic cell lines (Figure S2 I-J). These results indicated that NDUFS3-induced RAB7-downregulation was mediated by other factors.

Subsequently, we analyzed the amount of several other proteins involved in the endocytic pathway such as dynein, a motor complex responsible for the movement of all endocytic compartments on microtubules and thus for their intracellular localization [2], Lysosomal Associated Membrane Protein 1 (LAMP1), a lysosomal glycoprotein highly abundant in the late endosomal and lysosomal membranes [39], the transcription factor EB (TFEB), which promotes lysosome biogenesis, autophagosome formation, and lysosome fusion [40], the ATPase H + Transporting V1 Subunit G1 (ATP6V1G1), a vacuolar H+-ATPase subunit regulated by the RAB7 effector RILP and responsible of lysosomal acidification [41] and, finally, RAB9, a GTPase involved in sorting lysosomal enzymes to late endosomes [42] (Fig. 4A-D). Interestingly, we found that all these proteins were downregulated in *NDUFS3*-silenced YAPC and MIA PaCa-2 cells compared to the relative controls (Fig. 4B, D). Instead, analysis of proteins involved in early endocytic steps or recycling, such as RAB4, RAB5, and RAB11, revealed no variation upon *NDUFS3* silencing in both cell lines (Fig. S3). Also, we didn't detect changes in microtubule-associated Protein 1 Light Chain 3-II (LC3-II) upon *NDUFS3* silencing in MIA PaCa-2 cells while a LC3-II downregulation was detected in YAPC cells, indicating a cell line-specific effect that calls for future investigation (Figure S3).

Furthermore, a live-cell imaging assay using the LysoTracker DND-99 probe was performed. As shown in Fig. 4E, we found in YAPC and MIA PaCa-2 *NDUFS3*-silenced cells a significant reduction in intensity, number, and size of acidic compartments (namely late endosomes and lysosomes) (Fig. 4F-K).

NDUFS3-mediated RAB7 downregulation induces an impairment of the late endocytic pathway

In light of the central role of RAB7 in regulating endocytic trafficking from early endosomes to the maturation and acidification of lysosomes [1, 2], since we observed an NDUFS3-mediated downregulation of RAB7 and, consequently, of other proteins of the late endocytic pathway, we decided to investigate cathepsin D maturation (Fig. 5A). Cathepsin D is a lysosomal protease synthesized as a preprocathepsin D precursor. The precursor is converted into procathepsin D (52 kDa) in the endoplasmic reticulum, and further processed in the acidic milieu of late endosomes and lysosomes, into the 44-kDa form, and finally into the 32-kDa mature form [43]. Procathepsin D is exported to the acidic extracellular environment in cancer cells promoting cancer cell metastasis [44]. Interestingly, the ratio between the two immature forms and the 32 kDa mature form was significantly altered in cells in both *NDUFS3*-silenced cell lines compared to controls, indicating that processing of Cathepsin D is impaired (Fig. 5B).

In order to confirm alterations of lysosomal activity suggested by the analysis of Cathepsin D maturation, we decided to perform a DQ-Green BSA assay (Fig. 5C) [45]. This dye is strongly self-quenched by conjugation to BSA, but digestion of BSA determines its dequenching and the release of dye-labeled protein fragments brightly fluorescent. Furthermore, DQ-BSA is insensitive to pH from pH 3–11 allowing the direct detection of proteolytic activity in situations where the pH is unknown and

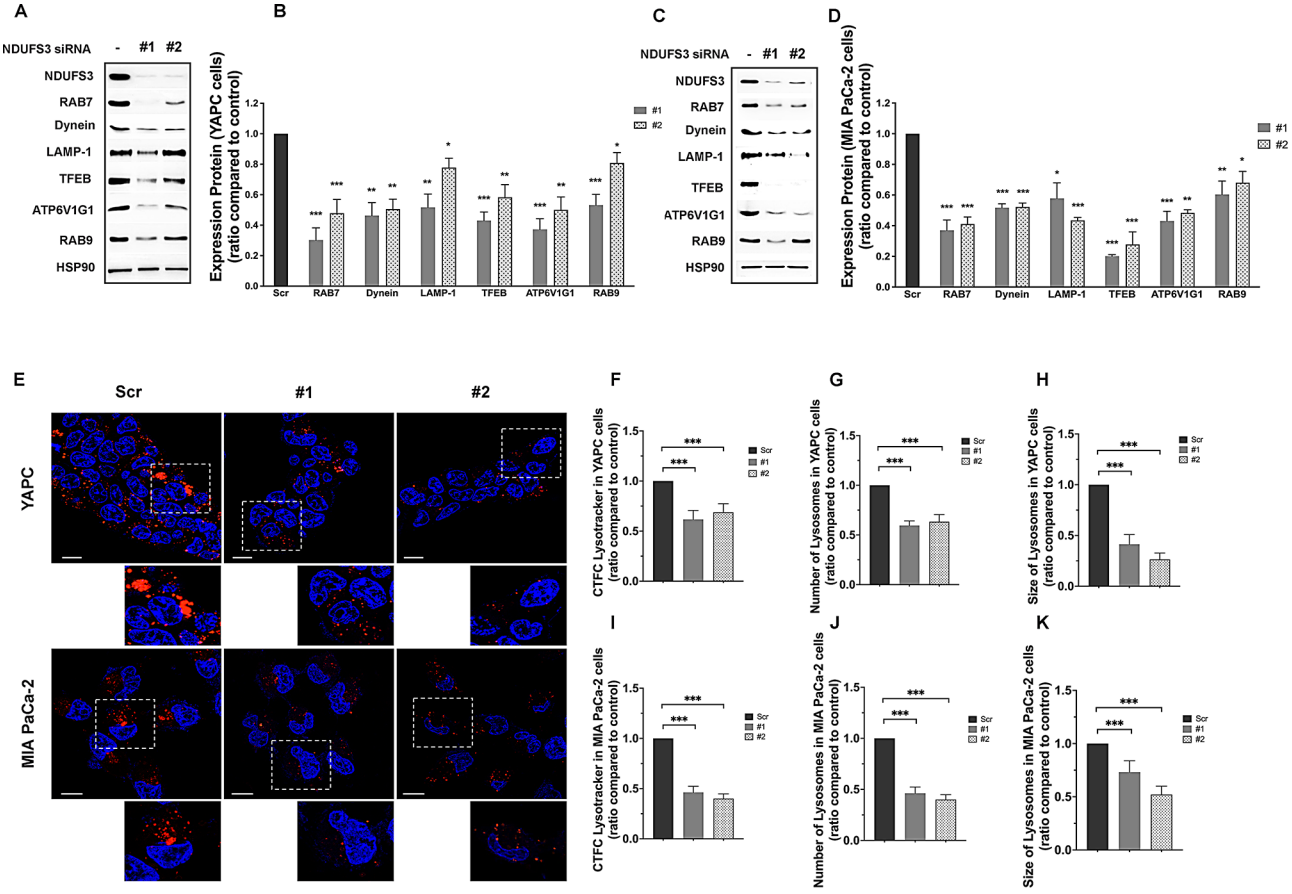

Fig. 4 Compromised late endocytic trafficking of *NDUFS3*-silenced pancreatic cancer cell lines. **(A-D)** Relative protein abundance of RAB7, dynein, LAMP-1, TFEB, ATP6V1G1, and RAB9 was assessed by Western blotting in YAPC and MIA PaCa-2 cells transfected with control RNA (Scr) or with two different *NDUFS3* siRNAs (indicated as #1 and #2). The antibody against NDUFS3 was used to check the efficiency of RNA interference (RNAi). Quantification of differences was performed by densitometric analysis, normalizing against HSP90, and it was reported as the ratio of *NDUFS3*-silenced samples (#1 and #2) compared to their Scr control. **(E)** Late endocytic acid compartments were live stained in *NDUFS3*-silenced YAPC and MIA PaCa-2 cells (indicated as #1 and #2) and relative Scr controls using LysoTracker DND-99 dye (red). Nuclei were labeled with PureBluTM Hoechst 33,342 Nuclear Staining Dye (blue). White boxes indicate zoomed areas below. Scale bar: 10 µm. **(F-K)** Corrected total cell fluorescence (CTCF), number and size of acid compartments were determined by ImageJ software in *NDUFS3*-silenced YAPC and MIA PaCa-2 cells and reported as the ratio compared to their Scr control. Each measure was obtained by analyzing at least 50 cells/samples from three or more independent experiments. Values are the mean ± SEM of at least three independent experiments. *$p \leq 0.05$, ** $p \leq 0.01$ and *** $p \leq 0.001$

cannot be controlled or where the pH is known to be low (e.g., endosomes and lysosomes). The analysis of DQ-BSA showed a strong decrease in dye fluorescence and in the number of puncta in YAPC (Fig. 5D-E), and in MIA PaCa-2 (Fig. 5F-G) cells upon silencing of *NDUFS3*, indicating that mitochondrial impairment is accompanied by lysosomal dysfunction.

Moreover, interestingly, in about 18% of MIA PaCa-2 cells silenced with siRNA#2, we found "megamitochondria" as defined previously as an effect of mitochondria-lysosomal dysregulation [46] (Fig. 5H-I).

Finally, to assess if effects on RAB7 and other endolysosomal proteins also occur when mitochondria are impeded by a different mechanism, we treated YAPC and MIA PaCA-2 cells with Rotenone, an inhibitor of CI, and with CCCP, a mitochondrial oxidative respiration uncoupler. In both cases, we found that RAB7 and LAMP-1 proteins are reduced in treated cells compared to controls (Fig. 5J-O). Interestingly, we observed a greater decrease in RAB7 levels in cells treated with rotenone (Fig. 5J), demonstrating that inhibition of CI can affect late endocytic trafficking, acting on RAB7.

NDUFS3-silenced RAB7-downregulated cells show reduced levels of vimentin protein along with a lower replicative and tumorigenic potential

Intermediate filaments are highly dynamic and fundamental for organelle positioning, transport, and function, thus being an important regulatory component of membrane traffic. Vimentin is a class III intermediate filament protein, and RAB7 is one of its interactors [47]. In particular, it was demonstrated that overexpression of RAB7

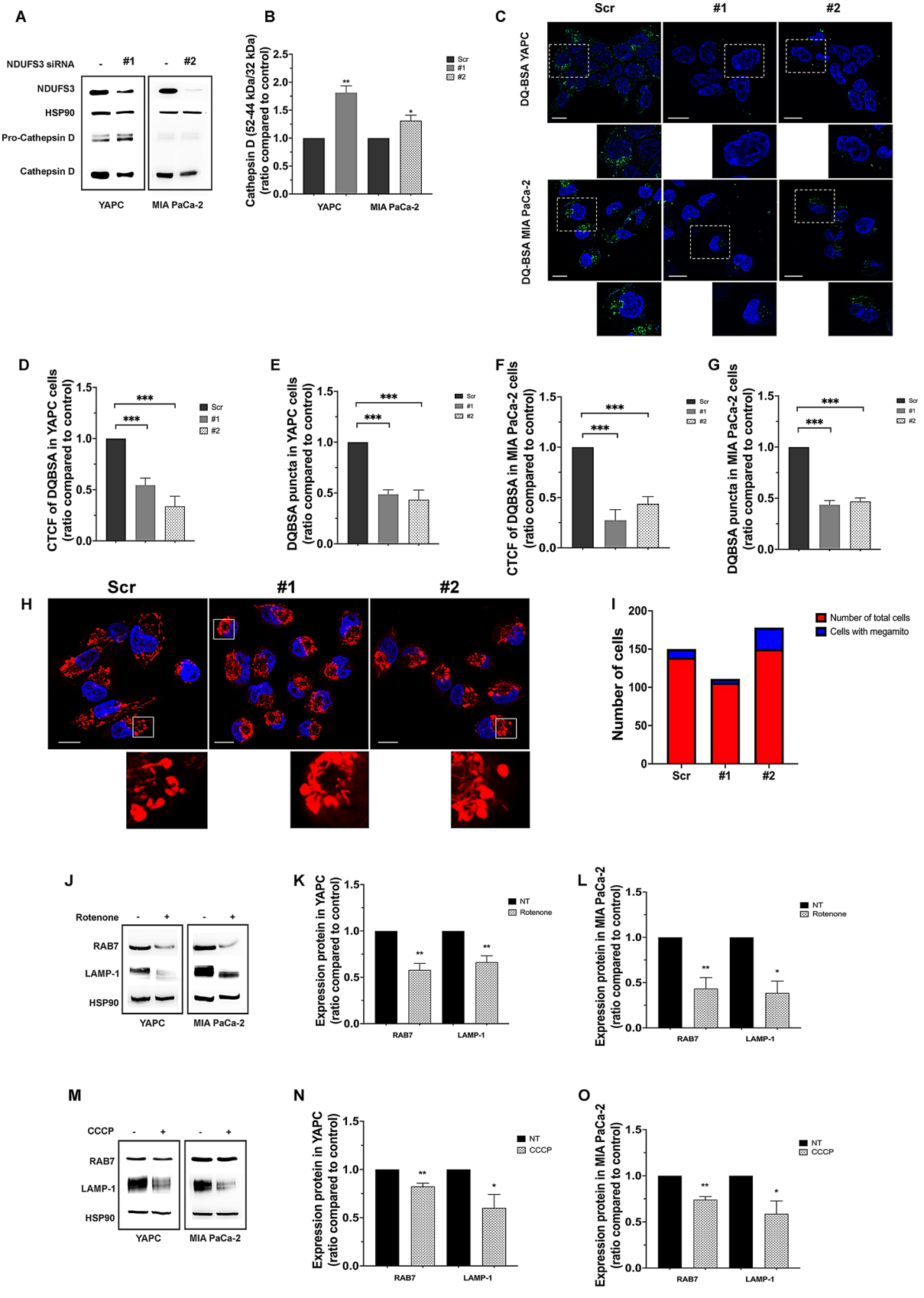

Fig. 5 (See legend on next page.)

(See figure on previous page.)

Fig. 5 Late endocytic pathway impairment in *NDUFS3*-silenced RAB7 downregulated cells. **(A)** The presence of Cathepsin D immature forms was evaluated by Western blot analysis on cell lysates from *NDUFS3*-silenced YAPC and MIA PaCa-2 cells (indicated as #1 and #2) and their respective controls using an anti-Cathepsin-D antibody. An antibody against NDUFS3 was used to verify silencing, while an antibody against HSP90 was used to verify correct loading. **(B)** Protein levels were quantified by densitometry with Image Lab Software version 6.0.1, and we quantified the ratio between immature forms (52/44 kDa) and mature form (32 kDa). The difference is reported as the ratio of *NDUFS3*-silenced cells compared to their Scr control. **(C)** Representative images of DQ-Green BSA assay in YAPC and MIA PaCa-2 silenced cells using *NDUFS3* siRNA #1 and #2 and their respective Scr controls. Nuclei were labeled with DAPI (blue). White boxes indicate zoomed areas below. Scale bar: 10 µm. **(D-G)** For each cell line, CTCF intensity and DQ-BSA puncta were quantified by ImageJ software. Data are reported as the ratio of *NDUFS3*-silenced samples (indicated as #1 and #2) compared to their Scr control. Measures were obtained by analyzing at least 50 cells/samples derived from three or more independent experiments. **(H)** Representative images of megamitochondria stained with MitoTracker Red CMXROS dye in MIA PaCa-2 cells *NDUFS3*-silenced (with siRNA #1 and #2) and relative control (Scr). Nuclei were labeled with DAPI (blue). White boxes indicate zoomed areas below. Scale bar: 10 µm. **(I)** Quantification of cells with megamitochondria in MIA PaCa-2 silenced cells and control compared with the total number of cells analyzed. (**J**) Relative protein abundance of RAB7 and LAMP-1 was assessed by Western blotting in YAPC and MIA PaCa-2 cells after treatment with Rotenone (1 µM) for 48 h and 72 h, respectively. An antibody against HSP90 was used to verify correct loading. **(K-L)** Protein levels were quantified by densitometry with Image Lab Software version 6.0.1. (**M**) Relative protein abundance of RAB7 and LAMP-1 was assessed by Western blotting in YAPC and MIA PaCa-2 cells after treatment with CCCP (10 µM) for 18 h. An antibody against HSP90 was used to verify correct loading. **(N-O)** Protein levels were quantified by densitometry with Image Lab Software version 6.0.1. Values are the mean ± SEM of at least three independent experiments. *$p \le 0.05$, ** $p \le 0.01$ and *** $p \le 0.001$

causes an increase in vimentin phosphorylation at different sites, determining its redistribution in the soluble fraction, whereas RAB7 silencing causes an increase in assembled vimentin present in the insoluble fraction [47].

In cancer, acquisition of the invasive phenotype is accomplished by several molecular alterations as a prelude to the Epithelial-to-Mesenchymal Transition (EMT) process and upregulation of the mesenchymal proteins, among which vimentin, are molecular changes involved in EMT and indicative of the invasion and metastasis potential of cancer cells [48].

To understand whether RAB7 downregulation in *NDUFS3*-silenced YAPC and MIA PaCa-2 cells could affect levels of vimentin, we have evaluated this protein by Western blot analysis (Fig. 6A, E). We found a significant reduction of vimentin expression in both *NDUFS3*-silenced RAB7-downregulated cellular models compared to their respective controls (Fig. 6B, F). Moreover, analysis of other proteins involved in EMT showed that, upon NDUFS3 silencing, N-cadherin and Slug were significantly downregulated in YAPC cells (Fig. 6A, C-D) while Snail was reduced in MIA PaCa-2 cells (Fig. 6E, G).

Then, we analyzed by zymography assay metalloprotease-2 (MMP-2) and metalloprotease-9 (MMP-9) activities. These extracellular endopeptidases are able to facilitate migration and metastasis by breaking down barriers formed by the extracellular matrix (ECM) [49]. A decrease in the activity of MMP-2 and MMP-9 was found in both *NDUFS3*-silenced RAB7-downregulated YAPC and MIA PaCa-2 cells (Fig. 6H) compared to their respective controls.

Interestingly, *NDUFS3*-silenced RAB7-downregulated cells displayed a significantly lower proliferation rate (Fig. 6I) and a decreased ability to form colonies in a clonogenic assay in anchorage-dependent growth conditions compared to control, which was concordant with a less aggressive phenotype (Fig. 6J-M). Furthermore, we performed a wound healing assay with *NDUFS3*-silenced RAB7-downregulated YAPC cells (Fig. 6N) and found a significantly reduced migration capacity in them after 24 h (Fig. 6O). Finally, we measured the number of migrating cells after *NDUFS3*-silencing in YAPC and MIA PaCa-2 cells by using seeding on a fluoroblok insert (Fig. 6P-Q), and we observed a significant reduction in this number for both cell lines compared to controls (Fig. 6R-S).

Therefore, these results suggest a potential reversion of the aggressive behavior in *NDUFS3*-silenced RAB7-downregulated cells.

RAB7 regulates vimentin expression and influences mitochondrial morphology in *NDUFS3*-silenced cells

In order to understand if observed changes in aggressive cancer phenotype were due to RAB7 downregulation or were only a consequence of *NDUFS3*-silencing, we performed the rescue of RAB7 expression level by transfecting HA-RAB7 protein in *NDUFS3*-silenced cells (Fig. 7A).

Interestingly, we observed a significant rescue of vimentin levels in YAPC and MIA PaCa-2 cells (Fig. 7A-C), indicating that RAB7 has a pivotal role in this process and can act as an oncogene in pancreatic cancer cells, modulating vimentin expression in the context of mitochondrial deregulation.

Furthermore, it was previously demonstrated that RAB7 promotes mitochondria-lysosome contact formation [5]. In particular, it was discovered that lysosomal contacts functionally mark sites of mitochondrial fission to allow the regulation of mitochondrial networks by lysosomes. Conversely, mitochondrial contacts regulate lysosomal RAB7 hydrolysis [5, 10]. Thereby, mitochondrial and lysosomal dynamics are bidirectionally regulated by mitochondria–lysosome contacts and may explain the dysfunction observed in both organelles in various human diseases. Here, we demonstrated an altered mitochondrial morphology in *NDUFS3*-silenced

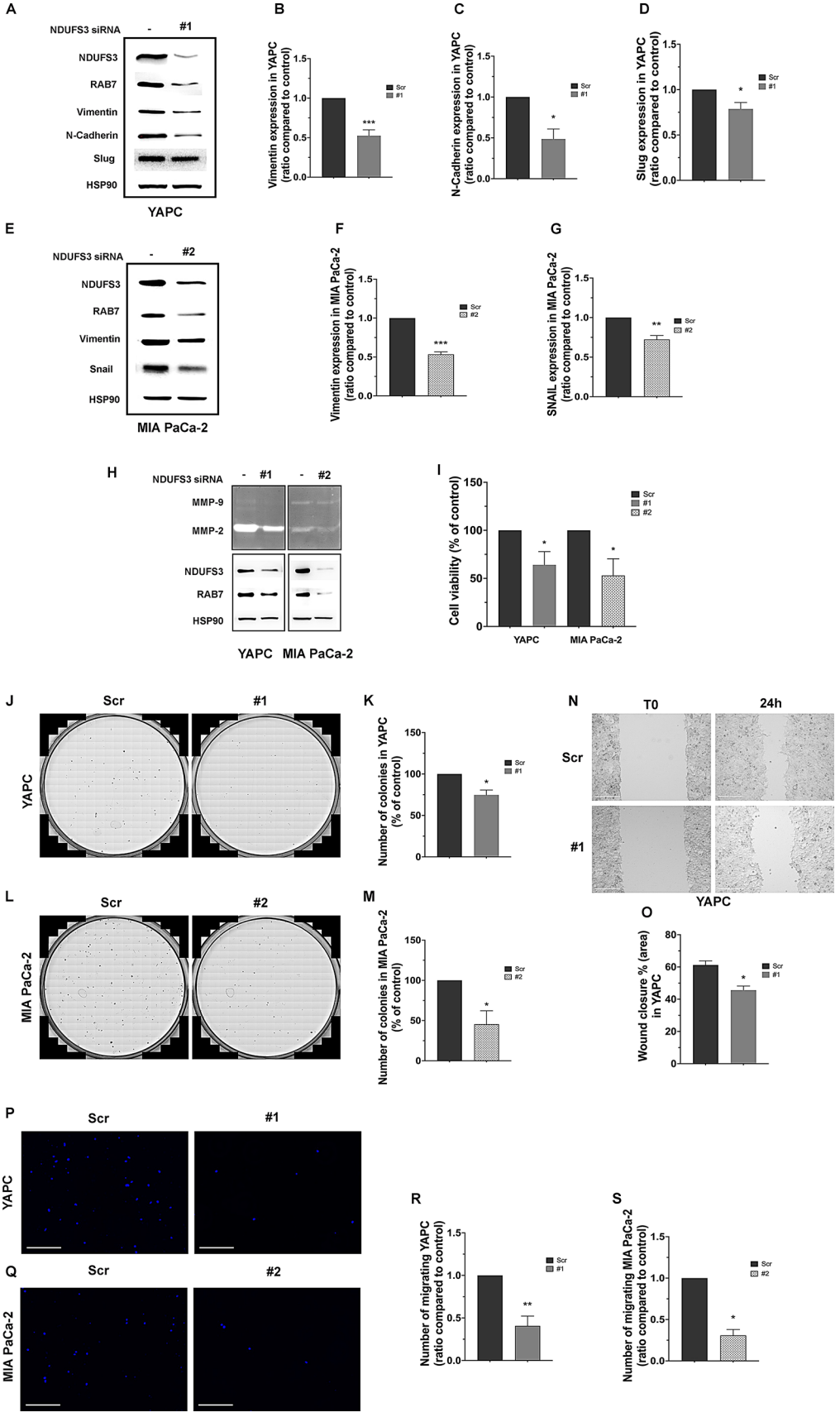

Fig. 6 (See legend on next page.)

(See figure on previous page.)

Fig. 6 *NDUFS3*-silenced RAB7-downregulated cells are characterized by a less aggressive phenotype. **(A)** Lysates from YAPC cells transfected with control RNA (Scr) and with *NDUFS3* siRNA#1 were subjected to SDS-PAGE and analyzed by immunoblotting using a specific antibody for vimentin, N-cadherin and Slug. An antibody against NDUFS3 was used to check the efficiency of silencing and an antibody against RAB7 was used to confirm the downregulation of this protein in silenced cells. **(B-D)** Relative abundance was quantified by densitometric analysis normalizing against HSP90 and it was reported as the ratio of *NDUFS3* RNAi samples (#1) compared to their Scr control. (**E**) Lysates from MIA PaCa-2 cells transfected with control RNA (Scr) and with *NDUFS3* siRNA#2 were subjected to SDS-PAGE and analyzed by immunoblotting using a specific antibody for vimentin and Snail. An antibody against NDUFS3 was used to check the efficiency of silencing and an antibody against RAB7 was used to confirm the downregulation of this protein in silenced cells. **(F-G)** Relative abundance was quantified by densitometric analysis normalizing against HSP90 and it was reported as the ratio of *NDUFS3* RNAi samples (#2) compared to their Scr control. **(H)** Conditioned medium from *NDUFS3*-silenced YAPC (siRNA#1) and MIA PaCa-2 (siRNA#2) and relative control (Scr) was used to assess the activity of secreted MMP-2 and MMP-9 by gelatin zymography. Lysates from YAPC and MIA PaCa-2 *NDUFS3*-silenced cells and their respective control cells were subjected to SDS-PAGE and analyzed by immunoblotting using an antibody against NDUFS3 to check the efficiency of RNAi, an antibody against RAB7 to confirm the downregulation of this protein in silenced cells, and an antibody against HSP90 to verify the correct loading. **(I)** Viability of YAPC and MIA PaCa-2 cells transfected with control RNA (Scr) and with *NDUFS3* siRNA#1 and siRNA#2, respectively. Data are presented normalized to T0 and the ratio of *NDUFS3* RNAi samples (#1 and #2) compared to their Scr control was reported. **(J-K)** Capacity of YAPC and **(L-M)** MIA PaCa-2 cells transfected with control RNA (Scr) and with *NDUFS3* siRNA#1 and siRNA#2, respectively, to form colonies in an anchorage-dependent manner. The ratio of *NDUFS3* RNAi samples compared to their Scr control was reported. **(N-O)** YAPC cells transfected with control RNA (Scr) and with *NDUFS3* siRNA#1 were imaged during the wound healing assay at an initial time point (T0) and 24 h after the scratch. Cell migration was measured as wound closure percentage after 24 h in Scr and in *NDUFS3* siRNA#1 YAPC cells. Scale bar: 200 µm. (**P-Q**) Nuclei of migrating YAPC and MIA PaCa-2 cells transfected with control RNA (Scr) and with *NDUFS3* siRNA#1 and siRNA#2, respectively, stained with 20 nM of PureBluTM Hoechst 33,342 Nuclear Staining Dye. Scale bar: 200 µm. **(R-S**) The mean number of migrating cells was calculated as the ratio of *NDUFS3* RNAi samples (#1 and #2) compared to their Scr control. Values are the mean ± SEM of at least three independent experiments. *$p \leq 0.05$, ** $p \leq 0.01$ and *** $p \leq 0.001$

cells (Fig. 2) in the presence of RAB7 downregulation. To understand whether RAB7 has a role in the observed alterations of mitochondrial morphology, as shown in Fig. 7, we rescued the level of RAB7 in *NDUFS3*-silenced RAB7-downregulated YAPC and MIA PaCa-2 cells. Thus, after GFP-RAB7 transfection, we performed mitochondrial staining using MitoTracker Red CMXROS dye (Fig. 7D and M). Raw images were processed to quantify the differences between GFP-RAB7 transfected *NDUFS3*-silenced cells and mock control. We observed that restored RAB7 levels were accompanied by a less fragmented mitochondrial morphology and an increase in mitochondrial network complexity (Fig. 7D-U). In particular, we observed in *NDUFS3*-silenced YAPC cells transfected with GFP-RAB7 a significant increase in mitochondria mean area (Fig. 7E) and perimeter (Fig. 7F), in the aspect ratio (Fig. 7G), in the form factor (Fig. 7H), in the branches for mitochondrion (Fig. 7J), in the total length of branches (Fig. 7K) as well as in the average branch length (Fig. 7L). In parallel, we found that in MIA PaCa-2 cells, the mean area (Fig. 7N), the mean perimeter (Fig. 7O), and the aspect ratio (Fig. 7P) of the mitochondria were increased after rescue of RAB7 expression in *NDUFS3*-silenced cells compared to controls. Furthermore, mitochondria, on average, showed a significant increase in the total length of branches upon RAB7 expression rescue (Fig. 7T). Finally, TFEB is the main regulator of lysosomal biogenesis [50] and, thus, to clarify the role of RAB7 in the impairment of late endocytic function induced by mitochondrial deficit, we analyzed TFEB levels upon RAB7 silencing and after rescue of RAB7 levels after *NDUFS3* downregulation (Figure S4A, C). We observed a significant reduction in TFEB expression after RAB7 RNAi (Figure S4B), but unchanged levels of this protein after RAB7 restoration in pancreatic *NDUFS3* silenced cells (Figure S4D-E). These results suggest that the effects on TFEB could be due to RAB7 downregulation, while the rescue of vimentin levels and of mitochondrial morphology (Fig. 7A, D and M) are only due to RAB7 in a TFEB-independent manner. This demonstrates the key role of RAB7 in the context of mitochondrial deficit, highlighting its influence on mitochondrial dynamic regulation.

Modulation of RAB7 influences the expression of mitochondrial transport chain subunits

In order to investigate if RAB7 has a specular role in influencing mitochondrial-lysosomal crosstalk, we decided to silence RAB7 in YAPC and MIA PaCa-2 cells and to evaluate expression levels of NDUFS3 and other mitochondrial proteins by Western blot analysis at different times (Fig. 8A and F).

In the first instance, we observed a significant reduction of RAB7 up to 7 days and 9 days for YAPC (Fig. 8A-B) and MIA PaCa-2 cells (Fig. 8F-G), respectively. In RAB7-silenced YAPC cells, we found, at the same time points, a significant reduction of NDUFS3, NDUFB8, and SDHB, proteins of complex I and complex II, respectively (Fig. 8A and C-E), except for NDUFS3 at the 3 days-time point. Similarly, we observed that the downregulation of RAB7 in MIA PaCa-2 cells induced a decrease in NDUFS3, SDHB, and NDUFB8 expression, mostly at 7 and 9 days (Fig. 8F and H-J). These data demonstrated that the downregulation of RAB7 can affect mitochondrial protein expression and can induce organelle deregulation.

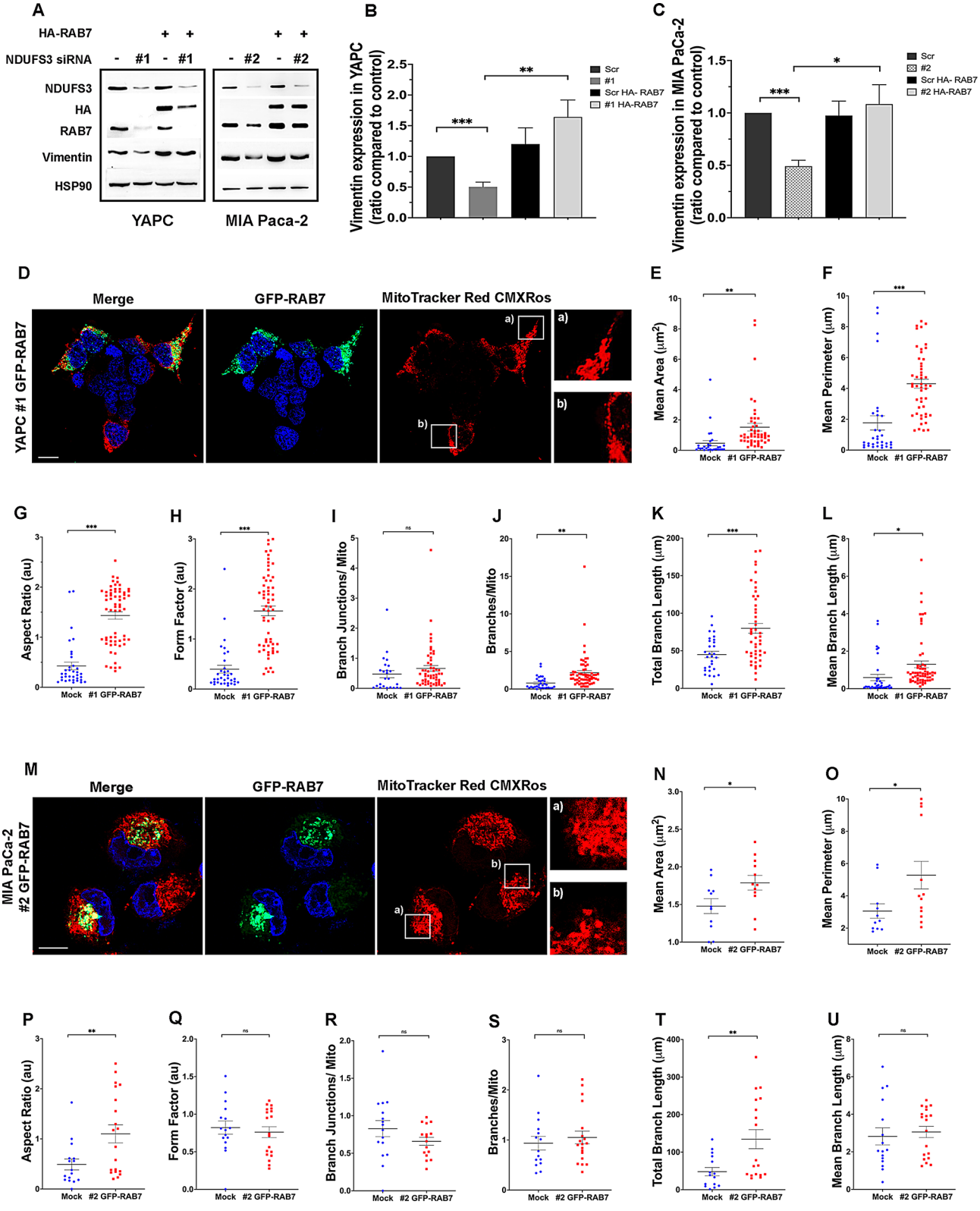

Fig. 7 (See legend on next page.)

(See figure on previous page.)

Fig. 7 Effect of rescued RAB7 levels on vimentin expression and mitochondrial morphology. **(A)** YAPC and MIA PaCa-2 *NDUFS3*-silenced cells and their respective controls were transfected with HA-RAB7 after 3 days of silencing. Levels of vimentin were analyzed by Western blot analysis respectively after 7 and 9 days from silencing. The same lysates were used to perform immunoblotting using antibodies against the HA tag to verify transfection, NDUFS3 to check the efficiency of RNAi, RAB7 to confirm the downregulation of this protein in silenced cells, HSP90 to show the correct loading. **(B-C)** Vimentin signal intensity was quantified by densitometric analysis by Image Lab Software version 6.0.1 in both cell lines and conditions and reported as the ratio of samples compared to their respective Scr control. **(D)** Representative image of GFP-RAB7 (green) and mitochondria (red, stained with MitoTracker Red CMXROS dye) in *NDUFS3*-silenced RAB7-downregulated YAPC cells transfected with GFP-RAB7 at day 3 of silencing. Nuclei were labeled with DAPI (blue). White boxes indicate zoomed areas on the right. In panel (a) mitochondria (red) in GFP-RAB7 transfected cells (green). In panel (b) mitochondria (red) in mock not transfected cells. Scale bar: 10 µm. The images were analyzed and quantified using the Mitochondria Analyzer in Fiji/ImageJ software (ImageJ). The measurements for **(E)** Mean Area (µm^2), **(F)** Mean Perimeter (µm), **(G)** Aspect Ratio (au), (**H**) Form Factor (au), **(I)** Branch Junctions/Mito, **(J)** Branches/Mito, **(K)** Total Branch Length (µm) and **(L)** Mean Branch Length (µm) are presented. The numbers of mitochondria analyzed are $n = 10{,}562$ from 30 images for the Mock control group, $n = 4555$ from 15 images for GFP-RAB7 transfected cells. **(M)** Representative image of GFP-RAB7 (green) and mitochondria (red) in MIA PaCa-2 *NDUFS3*-silenced RAB7-downregulated cells transfected with GFP-RAB7 at day 3 of silencing. Mitochondria were stained with MitoTracker Red CMXROS dye. Nuclei were labeled with DAPI (blue). White boxes indicate zoomed areas on the right. In panel (a) mitochondria (red) in GFP-RAB7 transfected cells (green). In panel (b) mitochondria (red) in mock not transfected cells. Scale bar: 10 µm. The images were analyzed and quantified using the Mitochondria Analyzer in Fiji/ImageJ software (ImageJ). The measurements for **(N)** Mean Area (µm^2), **(O)** Mean Perimeter (µm), **(P)** Aspect Ratio (au), (**Q**) Form Factor (au), **(R)** Branch Junctions/Mito, **(S)** Branches/Mito, **(T)** Total Branch Length (µm) and **(U)** Mean Branch Length (µm) are presented. The numbers of mitochondria analyzed are $n = 4754$ from 19 images for the Mock control group, and $n = 2119$ from 20 images for GFP-RAB7 transfected cells transfected cells. Values are the mean ± SEM of at least three independent experiments. Abbreviation: ns: not significant. *$p \le 0.05$, ** $p \le 0.01$ and *** $p \le 0.001$

Discussion

The mechanisms of communication between mitochondria and lysosomes and the impact that the alteration of one organelle could have on the integrity of the other may contribute to the development of pathologies deserving attention [10]. A key stress component in the cell is metabolism that allows to redirect fuels to generate energy or to convert it into building blocks. Thus, anabolism and catabolism rely heavily on mitochondria and lysosomes which are also regulators of metabolic activity across the cells. The assessment of the endocytic status in the context of mitochondrial deregulation and its implication in tumorigenesis and cancer progression has been up to now poorly investigated.

In this work, we have analyzed the endocytic pathway in *NDUFS3*-silenced pancreatic cancer cells in order to investigate the impact on of late endocytic pathway and, in particular on lysosomes. *NDUFS3* is a nuclear-encoded mitochondrial gene, whose ablation was reported to impair CI function [18]. It is necessary to premise that, in the first instance, we have assessed the effect of transient silencing of *NDUFS3* on mitochondria. Indeed, this protein is essential to CI assembly and mitochondrial function [38], but transient silencing may not be enough to induce functional effect because of the polyploidy nature of mitochondria and the existence of several compensatory mechanisms [51, 52]. Thus, after performing RNA interference for different times, we chose the 7 and 9 day time points for YAPC and MIA PaCa-2 cells, respectively, to establish whether prolonged low levels of NDUFS3 protein may affect mitochondrial function. Interestingly, analyses of the expression of mitochondrial respiratory chain subunits, mitochondrial function, and abundance demonstrated that *NDUFS3* transient silencing is sufficient to affect mitochondrial physiology.

After the assessment of cellular models, we concentrated our attention on the role of RAB7, a key factor in the regulation of the late endocytic pathway. Emerging evidence suggests that this protein has many roles in mitochondrial homeostasis and processes [3, 6–8]. Moreover, RAB7 is already known as the main actor of mitochondria-lysosomes communication regulation [4, 5]. Nevertheless, although we recently demonstrated that in ovarian cancer cells, defects in mitochondria-lysosome communication, caused by a downregulation of RAB7, can influence the response to chemotherapy through the modulation of mitochondria-derived vesicle (MDV) secretion [9], most of the studies were concentrated on its role in neurodegenerative disease [10] and the role of RAB7 in the context of dysfunctional mitochondria in cancer has not yet been clarified.

Pancreatic ductal adenocarcinoma (PDAC) is a highly aggressive malignancy, representing one of the leading causes of cancer-related death, with a 5-year relative survival rate of 12% and a progressive annual increase in the number of diagnoses due to its challenging diagnosis and limited treatment options [53, 54]. RAB7 expression was described as a prognostic factor of poor diagnosis in PDAC [55] and mitochondrial dysfunction is widely described in PDAC [56]. Indeed, pancreatic cancer metabolism was reported as highly heterogeneous with different metabolic behaviors between the primary tumor and metastasis [57].

Thus, despite the enormous progress achieved in the past years, the identification of an effective cancer therapy remains today one of the main challenges of cancer research, in particular for PDAC. It is increasingly clear that not only cancer cells but also the tumor microenvironment (TME) is essential to guarantee neoplastic formation and proliferation [58, 59] and this is particularly true in pancreatic cancer [60]. To this purpose, it

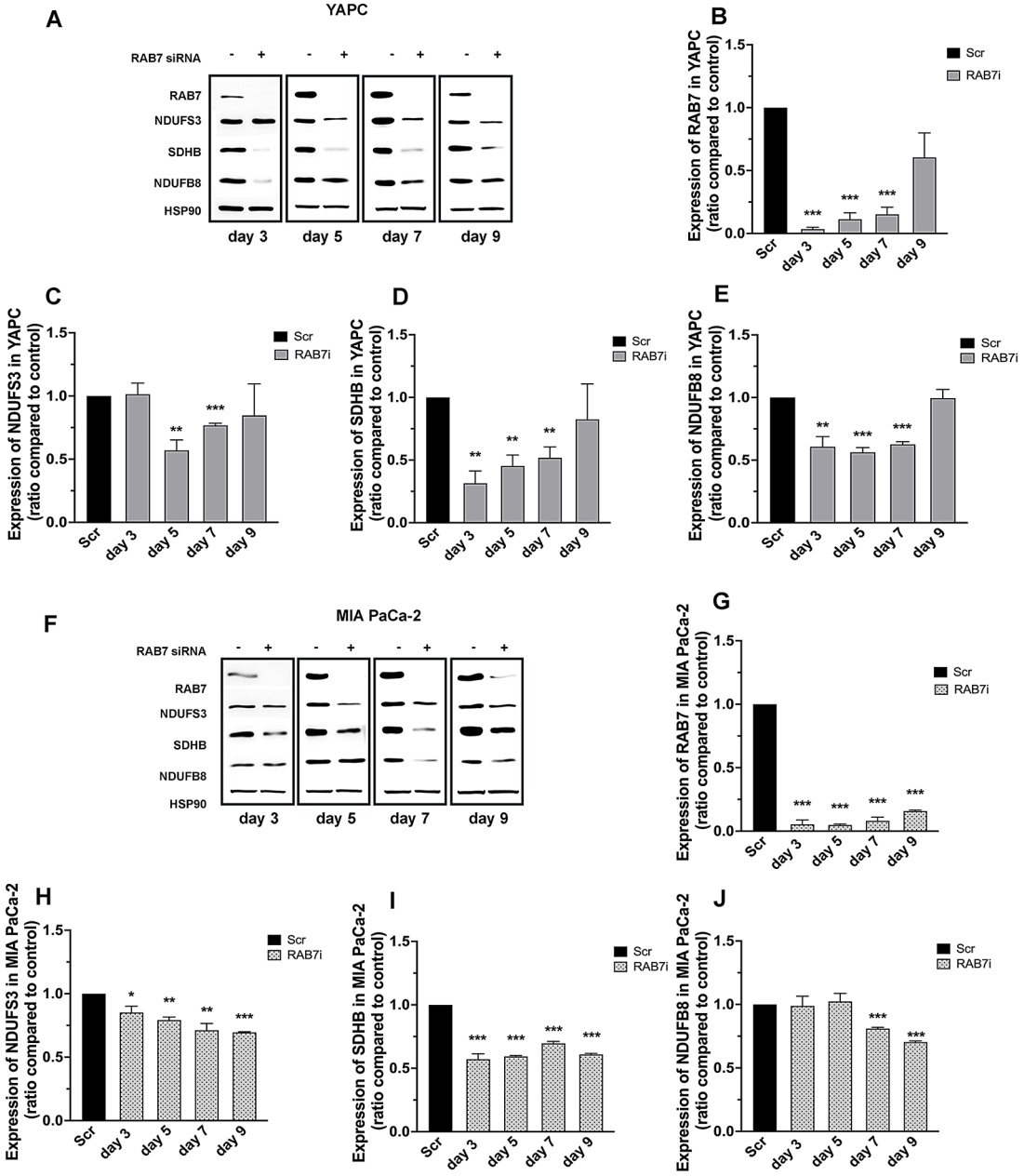

Fig. 8 The effect of the RAB7 silencing on mitochondrial proteins. **(A)** Lysates from RAB7-silenced YAPC cells at different time points (3, 5, 7, 9 days after RAB7 RNA interference) and the respective Scr control were subjected to SDS-PAGE and analyzed by immunoblotting using specific antibodies for NDUFS3, NDUFB8, SDHB. **(B)** The signal intensity of RAB7 was quantified by densitometric analysis by Image Lab Software version 6.0.1, normalizing against HSP90 to show the efficiency of silencing at different time points. **(C-E)** Relative abundances of NDUFS3, SDHB, and NDUFB8 were quantified by densitometric analysis by Image Lab Software version 6.0.1, normalizing against HSP90. **(F)** Lysates from MIA PaCa-2 RAB7-silenced cells at different time points (3, 5, 7, 9 days after RAB7 RNA interference) and the respective Scr control were subjected to SDS-PAGE and analyzed by immunoblotting using specific antibodies for NDUFS3, NDUFB8, SDHB. **(G)** The signal intensity of RAB7 was quantified by densitometric analysis by Image Lab Software version 6.0.1, normalizing against HSP90 to show the efficiency of silencing at different time points. **(H-J)** Relative abundances of NDUFS3, SDHB, and NDUFB8 were quantified by densitometric analysis by Image Lab Software version 6.0.1, normalizing against HSP90. Protein expression was reported as the ratio of RAB7-silenced samples compared to their Scr control. Values are the mean ± SEM of at least three independent experiments. *$p \leq 0.05$, ** $p \leq 0.01$ and *** $p \leq 0.001$

was previously demonstrated that complete CI ablation induced the acquisition of benign and low-proliferating phenotype in different cancer types, subsequently accomplished by an adaptive survival response tumor associated macrophages (TAM)-mediated [18]. In this work, we perform transient silencing of *NDUFS3* to avoid this adaptive response and emulate in vitro effects of the inhibitors of CI, actually objects of clinical trials for cancer treatment [57, 61, 62]. It was previously demonstrated that in cells in which the expression of *NDUFS3* could be repressed by doxycycline (Dox) in a tetracycline (Tet)-off system, the effect on CI ablation was evident after about 8 days of exposure [38]. Accordingly, for most experiments, we performed the *NDUFS3* transient RNA interference for up to 7 days and 9 days for YAPC and MIA PaCa-2 cells, respectively, and these time points correspond to the strongest RAB7 downregulation.

In this work, for the first time, we show the role of RAB7 in the regulation of mitochondria and lysosome crosstalk in pancreatic cancer cells. We found that impairment of the late endocytic pathway occurs in a context of mitochondrial deficit. We demonstrated that RAB7 transcriptional levels, proteasomal degradation, and protein stability were unchanged when NDUFS3 was silenced, and we hypothesize that RAB7 expression levels could be modulated by its secretion in extracellular vesicles (EVs), as described in the occurrence of a synergistic dysfunction of mitochondria and lysosomes [9].

In particular, RAB7 downregulation is accompanied by a decrease in several endocytic protein amounts and by dysfunctional lysosomal activity. Several works described RAB7 as an oncogene and oncosuppressor based on cellular and tissue context [24] and it was demonstrated that downregulation of RAB7 in myeloid-derived suppressor cells (MDSCs) determined glucose metabolic reprogramming, the increase of healthy mitochondria, and abrogation of tumor growth and invasion in vivo [63, 64]. In contrast, a reduced level of RAB7 in prostate cancer is needed to prevent lysosome localization next to the plasma membrane and consequent secretion of proteases avoiding larger tumor formation in vivo and increased invasive capability into surrounding tissue [65, 66]. In our work, the downregulation of RAB7 is directly associated with MMP secretion, which can be responsible for ECM degradation and TME activation. Moreover, when we modulated NDUFS3 levels, the decrease in RAB7 was accompanied by reduced expression of its interactor vimentin [47], by the decrease in other EMT proteins, such as N-Cadherin, Slug, and Snail proteins, by reduced viability of cancer cells, by a decrease in colony formation, migration and invasiveness. All these data indicate the acquisition of a low proliferating behavior in silenced cells, possibly determined by RAB7 downregulation. In fact, the rescue of RAB7 expression in *NDUFS3*-silenced cell models determines the corresponding rescue of vimentin expression levels, independently of *NDUFS3* expression, suggesting a pivotal role of RAB7 in the regulation of cancer aggressive phenotype. Moreover, to support our hypothesis, we demonstrated that rescue of RAB7 expression is also associated with restoring mitochondrial morphology. At the same time, RAB7 silencing is able alone to decrease the levels of some proteins of the electron chain mitochondrial subunits, supporting its role in mitochondrial homeostasis.

Altogether, our results demonstrate that in the context of mitochondrial deficit, RAB7 can be the needle of balance in the regulation of mitochondrial and lysosomal homeostasis and its imbalance can influence cancer behavior. This opens a therapeutics perspective in which the use of mitochondria complex inhibitors, such as metformin [21–23] coadjuvated by treatment with inhibitors of RAB7 function, might represent a potential strategy for pancreatic cancer treatment to reach synthetic lethality.

Conclusions

We were able, through transient silencing of *NDUFS3*, to induce not only mitochondrial deficit but also lysosomal dysfunction, emulating synergistic organelle impairment, which often characterizes cancer cells. In particular, in this work, we focused our attention on pancreatic cell models, and we found that in the context of mitochondrial deregulation, RAB7 is a key determinant of cancer cells' aggressive behavior (Fig. 9).

In fact, although it is already known that RAB7 controls many cellular pathways among which endocytosis and autophagy but also a number of mitochondrial pathways, the novelty of this work is the demonstration that mitochondrial dysfunction can act on RAB7, the key factor of endocytic trafficking, and that expression of RAB7 is able to revert the effects of mitochondria deregulation.

Furthermore, it is known that RAB7 can act as an oncosuppressor and oncogene in different tissue and cancer contexts, and the definition of its role as an oncogene in these pancreatic cell models adds a further important tile in the knowledge of this aggressive cancer.

Our principal perspective will be to reproduce this model in vivo to confirm our observations. Furthermore, this work provides the basis for hypothesizing future approaches in which synergistic inhibition of

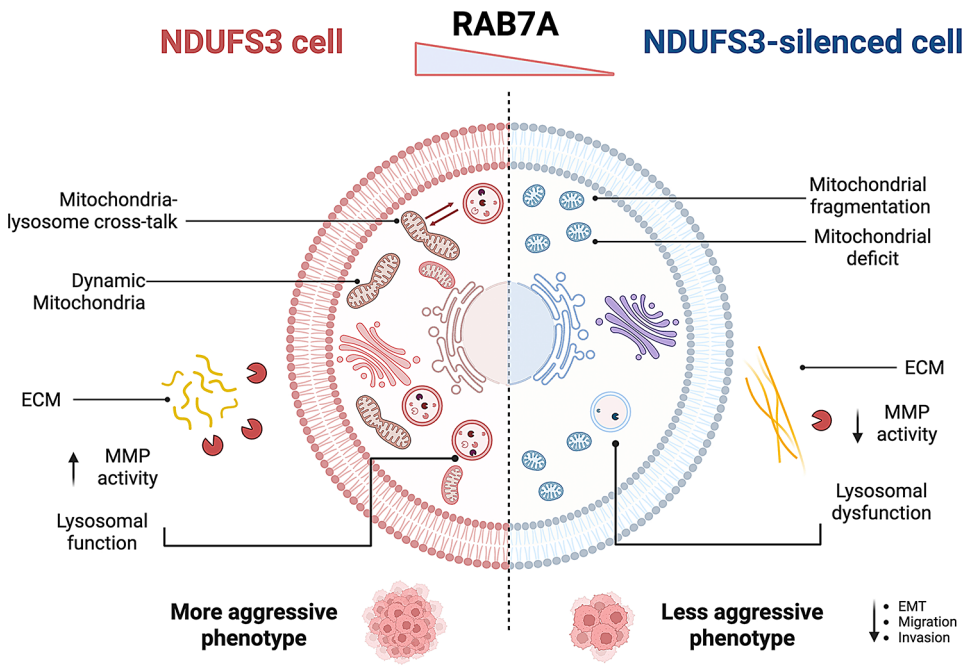

Fig. 9 Schematic representation of the molecular model. In pancreatic cancer cellular models, transient silencing of the nuclear-encoded mitochondrial *NDUFS3* gene, a subunit of Complex I, causes a mitochondrial deficit. The main regulator of mitochondria-lysosomes crosstalk is RAB7, a small GTPase with a pivotal role in late endocytic trafficking and lysosomal biogenesis. *NDUFS3* silencing induces downregulation of RAB7 expression with consequent impairment of mitochondria-lysosome communication, lysosomal function, and mitochondrial dynamics. The ultimate effects of lysosomal and mitochondrial synergistic deficit are a decrease of MMP activity, of EMT protein expression, and reduced migration and invasion potential, determining the acquisition of a less cancer-aggressive phenotype

mitochondrial and lysosomal function can represent a potential therapeutic strategy to treat pancreatic cancer.

Abbreviations

AR	Aspect Ratio
ATP	Adenosine Triphosphate
ATP6V1G1	ATPase H + Transporting V1 Subunit G1
BCA	Bicinchoninic Acid
CCCP	Carbonyl cyanide m-chlorophenyl hydrazone
CHX	Cycloheximide
CI	Mitochondrial complex I
CLSM	Confocal Laser Scanning Microscope
CTCF	Correct Total Cell Fluorescence
DAPI	4',6-diamidino-2-phenylindole
Dox	Doxycycline
DQ-BSA	Self-Quenched BODIPY Dye Conjugates of Bovine Serum Albumin
ECM	Extracellular matrix
EE	Early endosomes
EMT	Epithelial-to-Mesenchymal Transition
FBS	Fetal Bovine Serum
FCCP	Carbonyl cyanide-p-trifluoromethoxyphenylhydrazone
FF	Form Factor
GTP	Guanosine Triphosphate
GTPase	Guanosine Triphosphatase
LAMP-1	Lysosomal Associated Membrane Protein 1
LE	Late endosomes
MDSCs	Myeloid-Derived Suppressor Cells
MDVs	Mitochondria-Derived Vesicles
MMP-2	Metalloprotease-2
MMP-9	Metalloprotease-9
NDUFB8	NADH: Ubiquinone Oxidoreductase Subunit B8
NDUFS3	NADH: Ubiquinone Oxidoreductase Core Subunit S3
OCR	Oxygen Consumption Rate
OXPHOS	Oxidative Phosphorylation
PBS	Phosphate Buffer
PCR	Polymerase Chain Reaction
PDAC	Pancreatic ductal adenocarcinoma
qRT-PCR	Quantitative Real Time PCR
RAB7	Ras-related in Brain 7
RNAi	RNA interference
Rot/AA	Rotenone/Antimycin A
SDHB	Succinate Dehydrogenase complex iron sulphur subunit B
siRNA	small interfering RNA
SRB	Sulforhodamine B
TAM	Tumor Associated Macrophages
TEM	Transmission Electron Microscopy
Tet	Tetracycline
TFEB	Transcriptional Factor EB
TME	Tumor microenvironment

Supplementary Information

The online version contains supplementary material available at https://doi.org/10.1186/s12964-025-02214-y.

Supplementary Material 1

Supplementary Material 2

Acknowledgements

Figure 9 was created using Biorender scientific image and illustration software at www.biorender.com.

Author contributions

C. B. and F. G. conceived the project, designed the experiments, and supervised the work. G.G., S.G., P.C., G.B., R.R. and F.G. performed most of the experiments including cell culture, gene silencing, Western blot analysis, functional assays and confocal microscopy. C.B., F.G., G.G. and S.G. analyzed

and interpreted the data. R.D.C performed TEM experiments and analysis. F.G. wrote the manuscript. All the authors critically revised the manuscript and approved the final version of the manuscript.

Funding
The research leading to these results has received funding from AIRC under IG 2021 - ID. 25795 project – P.I. Cecilia Bucci.

Data availability
Data is provided within the manuscript or supplementary information files.

Declarations

Ethical approval and consent to participate
Not applicable.

Consent for publication
All authors gave their consents to publish this work.

Competing interests
The authors declare no competing interests.

Author details
[1]Department of Experimental Medicine, University of Salento, Via Provinciale Lecce-Monteroni n. 165, Lecce 73100, Italy
[2]Department of Biological and Environmental Sciences and Technologies, University of Salento, Via Provinciale Lecce-Monteroni n. 165, Lecce 73100, Italy
[3]Institute for Microelectronics and Microsystems (IMM), CNR, Via Provinciale Lecce-Monteroni, Lecce 73100, Italy
[4]Center for Biomolecular Nanotechnologies, Istituto Italiano di Tecnologia, Arnesano 73010, Italy

Received: 11 December 2024 / Accepted: 23 April 2025
Published online: 14 May 2025

References

1. Bucci C, Thomsen P, Nicoziani P, McCarthy J, van Deurs B. Rab7: a key to lysosome biogenesis. Mol Biol Cell. 2000;11(2):467–80.
2. Guerra F, Bucci C. Multiple roles of the small GTPase Rab7. Cells. 2016;5(3):E34.
3. Yamano K, Fogel AI, Wang C, van der Bliek AM, Youle RJ. Mitochondrial Rab gaps govern autophagosome biogenesis during mitophagy. Elife. 2014;3:e01612.
4. Wong YC, Peng W, Krainc D. Lysosomal regulation of Inter-mitochondrial contact fate and motility in Charcot-Marie-Tooth type 2. Dev Cell. 2019;50(3):339–54. e4.
5. Wong YC, Ysselstein D, Krainc D. Mitochondria-lysosome contacts regulate mitochondrial fission via RAB7 GTP hydrolysis. Nature. 2018;554(7692):382–6.
6. Pan ZN, Pan MH, Sun MH, Li XH, Zhang Y, Sun SC. RAB7 GTPase regulates actin dynamics for DRP1-mediated mitochondria function and spindle migration in mouse oocyte meiosis. FASEB J. 2020;34:9615–27.
7. Cioni J-M, Lin JQ, Holtermann AV, Koppers M, Jakobs MAH, Azizi A, et al. Late endosomes act as mRNA translation platforms and sustain mitochondria in axons. Cell. 2019;176:56–72.
8. Matheoud D, Sugiura A, Bellemare-Pelletier A, Laplante A, Rondeau C, Chemali M, et al. Parkinson's Disease-Related proteins PINK1 and parkin repress mitochondrial antigen presentation. Cell. 2016;166:314–27.
9. Gagliardi S, Mitruccio M, Di Corato R, Romano R, Aloisi A, Rinaldi R, et al. Defects of mitochondria-lysosomes communication induce secretion of mitochondria-derived vesicles and drive chemoresistance in ovarian cancer cells. Cell Commun Signal. 2024;22(1):165.
10. Deus CM, Yambire KF, Oliveira PJ, Raimundo N. Mitochondria-Lysosome crosstalk: from physiology to neurodegeneration. Trends Mol Med. 2020;26(1):71–88.
11. Shteinfer-Kuzmine A, Verma A, Arif T, Aizenberg O, Paul A, Shoshan-Barmaz V. Mitochondria and nucleus cross-talk: signaling in metabolism, apoptosis, and differentiation, and function in cancer. IUBMB Life. 2021;73(3):492–510.
12. Díaz P, Sandoval-Bórquez A, Bravo-Sagua R, Quest AFG, Lavandero S. Perspectives on organelle interaction, protein dysregulation, and Cancer disease. Front Cell Dev Biology. 2021;9:613336.
13. Martinez-Carreres L, Nasrallah A, Fajas L. Linking powerhouses to suicidal bags. Front Oncol. 2017;7:204.
14. Vasan K, Werner M, Chandel NS. Mitochondrial metabolism as a target for Cancer therapy. Cell Metab. 2020;32(3):341–52.
15. Wang SF, Tseng LM, Lee HC. Role of mitochondrial alterations in human cancer progression and cancer immunity. J Biomed Sci. 2023;30(1):61.
16. Luo Z, Eichinger KM, Zhang A, Li S. Targeting cancer metabolic pathways for improving chemotherapy and immunotherapy. Cancer Lett. 2023;575:216396.
17. Xiao Y, Yu TJ, Xu Y, Ding R, Wang YP, Jiang YZ, et al. Emerging therapies in cancer metabolism. Cell Metab. 2023;35(8):1283–303.
18. Kurelac I, Iommarini L, Vatrinet R, Amato LB, De Luise M, Leone G, et al. Inducing cancer indolence by targeting mitochondrial complex I is potentiated by blocking macrophage-mediated adaptive responses. Nat Commun. 2019;10(1):903.
19. Wheaton WW, Weinberg SE, Hamanaka RB, Soberanes S, Sullivan LB, Anso E, et al. Metformin inhibits mitochondrial complex I of cancer cells to reduce tumorigenesis. Elife. 2014;3:e02242.
20. Mahmood M, Liu EM, Shergold AL, Tolla E, Tait-Mulder J, Huerta-Uribe A, et al. Mitochondrial DNA mutations drive aerobic Glycolysis to enhance checkpoint Blockade response in melanoma. Nat Cancer. 2024;5(4):659–72.
21. Yoshida J, Ohishi T, Abe H, Ohba SI, Inoue H, Usami I, et al. Mitochondrial complex I inhibitors suppress tumor growth through concomitant acidification of the intra- and extracellular environment. iScience. 2021;24(12):103497.
22. AbuEid M, McAllister DM, McOlash L, Harwig MC, Cheng G, Drouillard D, et al. Synchronous effects of targeted mitochondrial complex I inhibitors on tumor and immune cells abrogate melanoma progression. iScience. 2021;24(6):102653.
23. Kurelac I, Cavina B, Sollazzo M, Miglietta S, Fornasa A, De Luise M, et al. NDUFS3 knockout cancer cells and molecular Docking reveal specificity and mode of action of anti-cancer respiratory complex I inhibitors. Open Biol. 2022;12(11):220198.
24. Guerra F, Bucci C. Role of the RAB7 protein in tumor progression and cisplatin chemoresistance. Cancers. 2019;11:1096.
25. Bairoch A. The Cellosaurus, a Cell-Line knowledge resource. J Biomol Tech. 2018;29(2):25–38.
26. De Santis MC, Gozzelino L, Margaria JP, Costamagna A, Ratto E, Gulluni F, et al. Lysosomal lipid switch sensitises to nutrient deprivation and mTOR targeting in pancreatic cancer. Gut. 2023;72(2):360–71.
27. Moro L, Simoneschi D, Kurz E, Arbini AA, Jang S, Guaragnella N, et al. Epigenetic Silencing of the ubiquitin ligase subunit FBXL7 impairs c-SRC degradation and promotes epithelial-to-mesenchymal transition and metastasis. Nat Cell Biol. 2020;22(9):1130–42.
28. Spinosa MR, Progida C, De Luca A, Colucci AM, Alifano P, Bucci C. Functional characterization of Rab7 mutant proteins associated with Charcot-Marie-Tooth type 2B disease. J Neurosci. 2008;28(7):1640–8.
29. Spinosa MR, Progida C, De Luca A, Colucci AMR, Alifano P, Bucci C. Functional characterization of Rab7 mutant proteins associated with Charcot-Marie-Tooth type 2B disease. J Neurosci. 2008;28(7):1640–8.
30. Guerra F, Girolimetti G, Beli R, Mitruccio M, Pacelli C, Ferretta A, et al. Synergistic effect of mitochondrial and lysosomal dysfunction in Parkinson's disease. Cells. 2019;8(5):E452.
31. Vergara D, Stanca E, Guerra F, Priore P, Gaballo A, Franck J, et al. beta-Catenin knockdown affects mitochondrial biogenesis and lipid metabolism in breast Cancer cells. Front Physiol. 2017;8:544.
32. Romano R, Rivellini C, De Luca M, Tonlorenzi R, Beli R, Manganelli F, et al. Alteration of the late endocytic pathway in Charcot-Marie-Tooth type 2B disease. Cell Mol Life Sci. 2020;78(1):351–72.
33. Valente AJ, Maddalena LA, Robb EL, Moradi F, Stuart JA. A simple ImageJ macro tool for analyzing mitochondrial network morphology in mammalian cell culture. Acta Histochem. 2017;119:315–26.
34. Chaudhry A, Shi R, Luciani DS. E87-e101. A pipeline for multidimensional confocal analysis of mitochondrial morphology, function, and dynamics in pancreatic β-cells. Am J Physiol Endocrinol Metab. 2020;318:E87–101.
35. Guerra F, Paiano A, Migoni D, Girolimetti G, Perrone AM, De Iaco P, et al. Modulation of RAB7A protein expression determines resistance to cisplatin through late endocytic pathway impairment and extracellular vesicular secretion. Cancers. 2019;11:E52.

36. Grada A, Otero-Vinas M, Prieto-Castrillo F, Obagi Z, Falanga V. Research techniques made simple: analysis of collective cell migration using the wound healing assay. J Invest Dermatol. 2017;137(2):e11–6.
37. Lackner LL. Shaping the dynamic mitochondrial network. BMC Biol. 2014;12:35.
38. D'Angelo L, Astro E, De Luise M, Kurelac I, Umesh-Ganesh N, Ding S, et al. NDUFS3 depletion permits complex I maturation and reveals TMEM126A/OPA7 as an assembly factor binding the ND4-module intermediate. Cell Rep. 2021;35(3):109002.
39. Eskelinen EL. Roles of LAMP-1 and LAMP-2 in lysosome biogenesis and autophagy. Mol Aspects Med. 2006;27(5–6):495–502.
40. Puertollano R, Ferguson SM, Brugarolas J, Ballabio A. The complex relationship between TFEB transcription factor phosphorylation and subcellular localization. EMBO J. 2018;37(11):e98804.
41. De Luca M, Romano R, Bucci C. Role of the V1G1 subunit of V-ATPase in breast cancer cell migration. Sci Rep. 2021;11(1):4615.
42. Kornfeld S. Structure and function of the mannose 6-phosphate/insulin- like growth factor II receptors. Annu Rev Biochem. 1992;61:307–30.
43. Richo G, Conner GE. Proteolytic activation of human procathepsin D. Adv Exp Med Biol. 1991;306:289–96.
44. Benes P, Vetvicka V, Fusek M. Cathepsin D–many functions of one aspartic protease. Crit Rev Oncol Hematol. 2008;68:12–28.
45. Voss EW Jr., Workman CJ, Mummert ME. Detection of protease activity using a fluorescence-enhancement globular substrate. Biotechniques. 1996;20(2):286–91.
46. Hao T, Yu J, Wu Z, Jiang J, Gong L, Wang B, et al. Hypoxia-reprogramed mega-mitochondrion contacts and engulfs lysosome to mediate mitochondrial self-digestion. Nat Commun. 2023;14(1):4105.
47. Cogli L, Progida C, Bramato R, Bucci C. Vimentin phosphorylation and assembly are regulated by the small GTPase Rab7a. Biochim Biophys Acta. 2013;1833(6):1283–93.
48. Girolimetti G, Guerra F, Iommarini L, Kurelac I, Vergara D, Maffia M, et al. Platinum-induced mitochondrial DNA mutations confer lower sensitivity to Paclitaxel by impairing tubulin cytoskeletal organization. Hum Mol Genet. 2017;26:2961–74.
49. Scheau C, Badarau IA, Costache R, Caruntu C, Mihai GL, Didilescu AC, et al. The role of matrix metalloproteinases in the Epithelial-Mesenchymal transition of hepatocellular carcinoma. Anal Cell Pathol (Amst). 2019;2019:9423907.
50. Settembre C, Di Malta C, Polito VA, Garcia Arencibia M, Vetrini F, Erdin S, et al. TFEB links autophagy to lysosomal biogenesis. Science. 2011;332(6036):1429–33.
51. Liu L, Li Y, Chen G, Chen Q. Crosstalk between mitochondrial biogenesis and mitophagy to maintain mitochondrial homeostasis. J Biomed Sci. 2023;30(1):86.
52. Ferrucci L, Guerra F, Bucci C, Marzetti E, Picca A. Mitochondria break free: Mitochondria-derived vesicles in aging and associated conditions. Ageing Res Rev. 2024;102:102549.
53. Siegel RL, Miller KD, Wagle NS, Jemal A. Cancer statistics, 2023. CA Cancer J Clin. 2023;73(1):17–48.
54. Halbrook CJ, Lyssiotis CA, Pasca di Magliano M, Maitra A. Pancreatic cancer: advances and challenges. Cell. 2023;186(8):1729–54.
55. Liu Q, Bai Y, Shi X, Guo D, Wang Y, Wang Y, et al. High RAS-related protein Rab-7a (RAB7A) expression is a poor prognostic factor in pancreatic adenocarcinoma. Sci Rep. 2022;12(1):17492.
56. Fu Y, Ricciardiello F, Yang G, Qiu J, Huang H, Xiao J et al. The role of mitochondria in the chemoresistance of pancreatic Cancer cells. Cells. 2021;10(3).
57. De Santis MC, Bockorny B, Hirsch E, Cappello P, Martini M. Exploiting pancreatic cancer metabolism: challenges and opportunities. Trends Mol Med. 2024;30(6):592–604.
58. Romano R, Picca A, Eusebi LHU, Marzetti E, Calvani R, Moro L, et al. Extracellular vesicles and pancreatic cancer: insights on the roles of MiRNA, LncRNA, and protein cargos in Cancer progression. Cells. 2021;10(6):1361.
59. Quail DF, Joyce JA. Microenvironmental regulation of tumor progression and metastasis. Nat Med. 2013;19(11):1423–37.
60. Romano R, Picca A, Eusebi LHU, Marzetti E, Calvani R, Moro L et al. Extracellular vesicles and pancreatic cancer: insights on the roles of MiRNA, LncRNA, and protein cargos in Cancer progression. Cells. 2021;10(6).
61. Brown JR, Chan DK, Shank JJ, Griffith KA, Fan H, Szulawski R et al. Phase II clinical trial of Metformin as a cancer stem cell-targeting agent in ovarian cancer. JCI Insight. 2020;5(11).
62. Molina JR, Sun Y, Protopopova M, Gera S, Bandi M, Bristow C, et al. An inhibitor of oxidative phosphorylation exploits cancer vulnerability. Nat Med. 2018;24(7):1036–46.
63. Ding X, Zhang W, Zhao T, Yan C, Du H. Rab7 GTPase controls lipid metabolic signaling in myeloid-derived suppressor cells. Oncotarget. 2017;8(18):30123–37.
64. Bronte V, Brandau S, Chen SH, Colombo MP, Frey AB, Greten TF, et al. Recommendations for myeloid-derived suppressor cell nomenclature and characterization standards. Nat Commun. 2016;7:12150.
65. Steffan JJ, Dykes SS, Coleman DT, Adams LK, Rogers D, Carroll JL, et al. Supporting a role for the GTPase Rab7 in prostate cancer progression. PLoS ONE. 2014;9:e87882.
66. Steffan JJ, Cardelli JA. Thiazolidinediones induce Rab7-RILP- MAPK-dependent juxtanuclear lysosome aggregation and reduce tumor cell invasion. Traffic. 2010;11:274–86.

Publisher's note